Cbx2 targets PRC1 to constitutive heterochromatin in mouse zygotes in a parent-of-origin dependent manner.

Mathieu Tardat[1,7], Mareike Albert[1,2,5,7], Rico Kunzmann[1,2], Zichuan Liu[1], Lilia Kaustov[3], Raphael Thierry[1], Shili Duan[3], Urszula Brykczynska[1,2,6], Cheryl H. Arrowsmith[3,4] and Antoine H.F.M Peters[1,2]

[1] Friedrich Miescher Institute for Biomedical Research, 4058 Basel, Switzerland

[2] Faculty of Sciences, University of Basel, 4056 Basel, Switzerland

[3] Princess Margaret Cancer Centre and Department of Medical Biophysics, University of Toronto, Toronto, Ontario M5S 1A8, Canada

[4]Structural Genomics Consortium, University of Toronto, Toronto, Ontario M5G 1L7, Canada

[5] Current address: Max Planck Institute of Molecular Cell Biology and Genetics, 01307 Dresden, Germany

[6] Current address: Novartis Institutes for Biomedical Research, 4002 Basel, Switzerland.

[7] These authors contributed equally to this work

Corresponding author: Antoine Peters

Phone: +41 61 6978761, Fax: +41 61 6973976, Email: antoine.peters@fmi.ch

Running title: Cbx2 controls targeting of PRC1 to heterochromatin

Keywords: Constitutive heterochromatin, Polycomb Repressive Complex 1, Cbx2, Hp1β, Chromo domain, AT-hook

SUMMARY

Polycomb repressive complexes PRC1 and PRC2 regulate expression of genes involved in proliferation and development. In mouse early embryos, however, canonical PRC1 localizes to paternal pericentric heterochromatin (pat-PCH), where it represses transcription of major satellite repeats. In contrast, maternal PCH (mat-PCH) is enriched for H3 lysine 9 tri-methylation (H3K9me3) and Hp1β. How PRC1 is targeted to pat-PCH yet excluded from mat-PCH has remained elusive. Here, we identify a PRC1 targeting mechanism that relies on Cbx2 and Hp1β. Cbx2 directs catalytically active PRC1 to PCH via its chromodomain (CD^{Cbx2}) and neighboring AT-hook (AT^{Cbx2}) binding to H3K27me3 and AT-rich major satellites, respectively. CD^{Cbx2} prevents AT^{Cbx2} from interacting with DNA at PCH marked by H3K9me3 and Hp1β. Loss-of-function studies show that Hp1β and not H3K9me3 prevents PRC1 targeting to mat-PCH. Our findings indicate that CD^{Cbx2} and AT^{Cbx2} separated by a short linker function together to integrate H3K9me3/HP1 and H3K27me3 states.

INTRODUCTION

In higher eukaryotes, various chromatin pathways evolved to organize the genome into different compartments comprising of euchromatin, facultative and constitutive heterochromatin and to regulate gene expression (Campos and Reinberg, 2009; Fodor et al., 2010). Within each pathway, a plethora of chromatin modifying enzymes and associated proteins collaborate to define distinct chromatin states. Constitutive heterochromatin is generally found at repetitive sequences, for example those flanking centromeres in a variety of organisms ranging from *Schizosaccharomyces pombe* to human. In mice, pericentromeric heterochromatin (PCH) domains are comprised of 234 bp long AT-rich DNA sequences, called major satellites, organized in tandem arrays of several Mb length (Vissel and Choo, 1989). PCH is characterized by DNA methylation as well as *Suv39h*-mediated H3K9me3 that is

bound by HP1 proteins which in turn recruit the Suv4-20h histone lysine methyltransferases (HMTs) to catalyze H4K20me2/3 (Lachner et al., 2001; Li et al., 1992; Peters et al., 2001; Schotta et al., 2004). Impairment of constitutive heterochromatin is associated with increased major satellite transcription, nuclear organization defects and improper chromosome condensation and segregation (Hahn et al., 2013; Peters et al., 2001).

Facultative heterochromatin is generally enriched for Polycomb group (PcG) proteins that robustly modify chromatin and suppress non-lineage specific gene expression, thereby safeguarding developmental potency in embryonic and tissue-specific stem cells, during cellular differentiation and even in the mammalian germ line (Aloia et al., 2013; Posfai et al., 2012; Yokobayashi et al., 2013). In mammals, PcG proteins function in two main families of complexes, referred to as PRC1 and PRC2, that catalyze mono-ubiquitination of histone H2A on lysine 119 (H2AK119ub1) and tri-methylation of histone H3 on lysine 27 (H3K27me3) respectively (Beisel and Paro, 2011). How PRCs are targeted to chromatin has been subject of intense research. For years, PRC2-mediated H3K27me3 was thought to recruit PRC1 via the CD of Cbx proteins (Cao et al., 2002). More recently, however, variant PRC1 (vPRC1) complexes lacking Cbx subunits were shown to be targeted in ESCs to unmethylated CpG-island containing promoters via the CXXC DNA-binding motif of Kdm2b, independently of H3K27me3. Moreover, catalytic activity of vPRC1 directed PRC2 recruitment, resulting in H3K27me3 deposition (Blackledge et al., 2014; Cooper et al., 2014; Kalb et al., 2014).

Intriguingly, deletion of the two *Suv39h* HMTs in mouse embryonic stem cells (*Suv39h* double null (dn) ESCs) or the three DNA methyltransferases (TKO ESCs) results in accumulation of H3K27me3 and/or H2AK119ub1 at PCH (Cooper et al., 2014; Peters et al., 2003; Saksouk et al., 2014) demonstrating plasticity between PcG complexes and components of the classical constitutive heterochromatin pathway. High resolution immunofluorescence (IF) and protein composition analyses of PCH in TKO ESCs suggest a possible direct role for DNA methylation in preventing vPRC1 recruitment to PCH, presumably by blocking Kdm2b binding to DNA (Cooper et al.,

2014; Saksouk et al., 2014). On the other hand, PRC2 recruitment seems to be constrained by components in the *Suv39h* pathway other than those involved in DNA methylation (Cooper et al., 2014; Peters et al., 2003). Then again, Saksouk et al. (2014) identified Bend3 as a methylation-sensitive DNA-binding protein that is required for H3K27me3 accumulation at PCH in *Suv39h* dn ESCs, likely in *Dnmt* TKO ESCs and possibly in early mouse embryos. Currently, it is unclear to what extent such molecular interplay observed in ESCs is relevant for mouse development.

Mouse early embryos represent a unique situation in which mat-PCH and pat-PCH, although present in the same cellular environment, are formatted in distinct manners that reflect different chromatin reprogramming histories during gametogenesis (Gill et al., 2012; Puschendorf et al., 2008). Whereas mat-PCH in zygotes is characterized by classical heterochromatin features, components of a maternally provided canonical PRC1 complex called “matPRC1” like Cbx2, Bmi1, Phc2 and Rnf2 label pat-PCH where they suppress transcription of major satellite transcripts (Puschendorf et al., 2008). Furthermore, matPRC1 associates with mat-PCH in *Suv39h2*$^{m-z+}$ zygotes which lacks H3K9me3. Thus, matPRC1 functions as a repressive back-up mechanism of the Suv39/HP1 pathway.

We also demonstrated that matPRC1 targeting to pat-PCH is unaffected in *Ezh2* $^{m-z+}$ embryos, suggesting a possible involvement of vPRC1 (Puschendorf et al., 2008). Then again, H3K27me3 is established normally at pat-PCH in zygotes deficient for *Rnf2* arguing against a role for vPRC1 in PRC2 recruitment to pat-PCH. Finally, despite major changes in euchromatic DNA methylation patterns, paternal PCH remains DNA methylated during early pre-implantation development (Arand et al., 2015; Inoue et al., 2011) pointing to different mechanisms of PRC1 recruitment to pat-PCH in early embryos versus ESCs.

Here we unravel the molecular mechanism underlying targeting of matPRC1 to pat-PCH and its exclusion from mat-PCH. We show that Cbx2 directly targets catalytically active matPRC1 to pat-PCH via its CD and an AT-hook DNA binding domain that bind to H3K27me3-modified nucleosomes and AT-rich major satellites. Our studies suggest that CD^{Cbx2} and AT^{Cbx2} connected by a short linker function as one

reader module that integrates the H3K9me3/HP1 and H3K27me3 chromatin states for DNA binding by the AT-hook. Increasing the affinity of CD^{Cbx2} for H3K9me3 by a single amino acid change enables Cbx2 binding to H3K9me3/Hp1β marked PCH. Likewise, loss of maternal *Hp1β* results in strong matPRC1 localization at mat-PCH, despite the presence of H3K9me3. We conclude that Hp1β and not H3K9me3 prevents matPRC1 from binding mat-PCH. These data assign an important function to Cbx2 and Hp1β in specifying target selectivity of matPRC1 during early embryonic development.

RESULTS

Canonical PRC1 marks constitutive heterochromatin in mouse early embryos

Several "canonical" matPRC1 components label pat-PCH which in zygotes is organized in a spherical configuration around nucleolar-precursor bodies (NPBs) (Puschendorf et al., 2008). Besides these cPRC1 members, transcripts for various vPRC1 subunits are also maternally provided to the early embryo (Figure S1A) (Park et al., 2013). To investigate whether such vPRC1 members localize to pat-PCH in late zygotes, we performed IF analysis for Rybp using a specific antibody (Figure S1B-D), and for an EGFP-tagged Pcgf1 for which we had injected mRNA in early zygotes. Both proteins are part of the vPRC1 complex, also containing Kdm2b and Bcor, which localizes to unmethylated CpG islands in ESCs (Blackledge et al., 2014; Gao et al., 2012; García et al., 1999) (Figure 1A). In contrast to cPRC1 subunits, we did not observe selective enrichment for either vPRC1 protein at pat-PCH though euchromatin of both pronuclei was labeled (Figure 1B). Nonetheless and despite the presence of DNA methylation (Figure S1E) we observed strong H2AK119ub1 labeling at pat-PCH arguing that these cPRC1 members, constituting matPRC1, are able to robustly modify chromatin at major satellites, classical sites of constitutive heterochromatin formation, irrespective of the local DNA methylation status.

Cbx2 mediates PRC1 targeting to constitutive heterochromatin in *Suv39h* dn ESCs

We previously showed that PRC1 localization at PCH is recapitulated in *Suv39h* dn ESCs when matPRC1 proteins Cbx2, Bmi1, and Phc2 are co-expressed with endogenous Rnf2 (Puschendorf et al., 2008). To investigate which of these matPRC1 members may target the complex to PCH, we expressed the proteins individually in wild-type (wt) and *Suv39h* dn ESCs and quantified their enrichment at chromocenters relative to euchromatin using IF imaging approaches (Figure 1C, S1F). In mouse nuclei, chromocenters represent clusters of PCH regions from different chromosomes (Guenatri et al., 2004). Despite comparable expression levels (Figure S1G), only Cbx2 was strongly enriched at chromocenters in *Suv39h* dn ESCs (Figure 1C). Next we examined whether Cbx2 targets functional PRC1 complexes to PCH in *Suv39h* dn ESCs. Indeed, we observed consistent labeling of chromocenters by endogenous Phc1 and Rnf2 proteins and H2AK119ub1 upon expression of Cbx2-EGFP (Figure 1D). Since wt and *Suv39h* dn ESCs show similar levels of PRC1 and PRC2 proteins, H2AK119ub1 and alkaline phosphatase activity (Figure S1H-I), these results are not a consequence of differences in availability of endogenous PRC1 proteins or differentiation status of the two cell lines.

In embryos, EGFP-tagged Cbx2 localized to pat-PCH in *Rnf2*$^{m-z+}$ zygotes though we did not observe recruitment of endogenous Bmi1 nor H2AK119ub1 enrichment at pat-PCH. These data argue that Cbx2-mediated assembly of PRC1 complexes at heterochromatin requires the Rnf2 subunit (Figure 1E) which is consistent with known protein-protein interactions between PRC1 components (Gao et al., 2012; García et al., 1999). Altogether, these data indicate that Cbx2 targets active cPRC1 complexes to major satellites in pre-implantation mouse embryos and ESCs that are characterized by absence of H3K9me3 and HP1 proteins.

Cbx2 targeting to PCH in *Suv39h* dn ESCs depends on both its chromo- and AT-hook domains

We next investigated which domain(s) in Cbx2 confer binding to PCH. Cbx2 harbors a chromo domain (CD^{Cbx2}) that preferentially binds to H3K27me3 (Bernstein et al., 2006; Kaustov et al., 2011). This mark is strongly and moderately enriched at pat-

PCH in zygotes and chromocenters in *Suv39h* dn ESCs, respectively (Peters et al., 2003; Santos et al., 2005). Cbx2 also contains a conserved AT-hook (AT) close to CD^{Cbx2} and two AT-hook like (ATL) motifs (Figure 2A-B). AT-hooks bind to the minor groove of AT-rich DNA sequences, while ATL sequences are unlikely to bind DNA (Reeves and Nissen, 1990). Crucially, mouse major satellites underlying PCH are AT-rich sequences. To identify the role of CD^{Cbx2} and the AT-hook in PCH targeting, we impaired their binding abilities by introducing point mutations and scored the enrichment of tagged proteins on PCH relative to euchromatin in *Suv39h* dn ESCs (Figure S2). Whereas Cbx2-EGFP was strongly enriched at PCH, heterochromatic enrichment was significantly reduced for the Cbx2-CD^{F12A}- and Cbx2-AT^{G78R}-EGFP proteins (Figure 2C-D), demonstrating that both domains contribute to PCH targeting. In contrast, point mutations in either or both ATL motifs did not impair PCH targeting (Figure S2C, S2D). PCH enrichment was completely lost upon double mutation of the CD and AT-hook, arguing that CD^{Cbx2} and AT^{Cbx2} together confer binding to PCH (Figure 2C-D).

To further investigate the role of CD^{Cbx2} and AT^{Cbx2} in the association of Cbx2 to chromatin we performed Fluorescence Recovery after Photobleaching (FRAP) experiments. We observed a four-fold lower half fluorescence recovery time for both Cbx2-CD^{F12A} and Cbx2-AT^{G78R} mutations, compared to wt Cbx2, indicating a less stable association with PCH and faster turnover upon mutation of CD or AT (Figure 2E).

Finally, we performed chromatin immunoprecipitation followed by quantitative PCR (ChIP-qPCR) to quantify the impact of CD and AT point mutations on Cbx2 occupancy at major satellites. We observed robust Cbx2-EGFP enrichment at major satellites using well-controlled ChIP-qPCR conditions (Figure S2E). Mutation of either the CD or the AT-hook reduced occupancy at PCH, with an almost complete loss upon double mutation (Figure 2F). These data indicate that the CD^{Cbx2} and AT^{Cbx2} contribute to a similar extent to the recruitment of Cbx2 to PCH in *Suv39h* dn ESCs.

Cbx2 targeting to hetero- and euchromatin in zygotes

In vivo, pat-PCH acquires H3K27me3 concurrent with replication (Albert and Peters, 2009). Nonetheless, matPRC1 localizes already to pat-PCH in decondensing sperm nuclei shortly after fertilization (Puschendorf et al., 2008) suggesting that AT^{Cbx2} drives matPRC1 targeting at this stage of development. To test this hypothesis, we treated ESCs and embryos with the small compound distamycin A which interferes with the binding of AT-hook containing proteins to AT-rich satellite sequences in mouse and *Drosophila* by intercalating into the minor groove of DNA (Radic et al., 1992). IF and ChIP-qPCR experiments confirmed that distamycin A reduces Cbx2-EGFP localization at chromocenters and major satellites in *Suv39h* dn ESCs while heterochromatic localization of H3K9me3 and Hp1β was unaffected in wt cells (Figure S3A-E). In early mouse zygotes, PCH localization of endogenous matPRC1 components Cbx2 and Rnf2 in decondensing sperm heads was effectively abrogated by distamycin A in a concentration dependent-manner (Figure 3A). Thus, these data demonstrate the importance of AT^{Cbx2} at the onset of development in heterochromatic targeting of matPRC1 in an H3K27me3 independent manner.

To assess the importance of CD^{Cbx2} and AT^{Cbx2} for matPRC1 targeting in later stage embryos, we microinjected mRNA of various Cbx2-EGFP reporter constructs into early mouse zygotes shortly after fertilization and cultured them until pro-nuclear stage 5 (PN5), just prior to the first cleavage division (Figure S3F). Full length Cbx2-EGFP was strongly enriched at pat-PCH, like the endogenous protein (Figure 3B) (Puschendorf et al., 2008). Unlike in *Suv39h* dn ESCs, however, the Cbx2-CD^{F12A} mutation did not affect localization to pat-PCH, suggesting a greater contribution of the AT-hook to PCH binding in zygotes. This finding is consistent with our previous results showing *Ezh2*-independent targeting of matPRC1 to pat-PCH (Puschendorf et al., 2008). Indeed, Cbx2-EGFP remains strongly enriched at pat-PCH in *Ezh2*$^{m-z+}$ zygotes in which absence of the maternal enzyme prevents H3K27me3 establishment on the paternal pronucleus (Figure 3C).

Similarly, the Cbx2-AT^{G78R} mutation did not significantly reduce pat-PCH enrichment in wt zygotes (Figure 3B) suggesting a strong compensatory mechanism provided by CD^{Cbx2}. To test this possibility, we analyzed the Cbx2-CD^{F12A}-AT^{G78R} double

mutant in wt zygotes and observed a complete loss of signal at pat-PCH (Figure 3B). We also did not detect a signal in euchromatin of both pronuclei. To exclude the possibility that the double mutant protein is instable in embryos (Figure S2B), we tested the AT^{G78R} construct in *Ezh2*$^{m-z+}$ zygotes which lack H3K27me3 in the paternal genome. Consistently, we lost Cbx2-AT^{G78R} localization at pat-PCH and euchromatin in *Ezh2*$^{m-z+}$ compared to control conditions (Figure 3C). Thus, in contrast to *Suv39h* dn ESCs, CD^{Cbx2} and AT^{Cbx2} are each sufficient for efficient Cbx2 targeting to pat-PCH in one-cell embryos. The latter could in part be due to higher H3K27me3 levels at pat-PCH in embryos versus *Suv39h* dn ESCs and/or to differences in chromatin accessibility affecting the ability of the AT-hook to bind DNA.

CD^{Cbx2} and AT^{Cbx2} mediate chromatin association

To explore the role of CD^{Cbx2} and AT^{Cbx2} in euchromatin binding, we performed co-immunoprecipitation of wt and mutant Cbx2-EGFP transfected into HEK293 cells and probed for their association with H3K27me3-modified nucleosomes (Figure 4A). Although all Cbx2-EGFP proteins associated with Rnf2, mutation of CD^{Cbx2} or AT^{Cbx2} resulted respectively in a strong and moderate reduction of immunoprecipitated H3K27me3-modified nucleosomes compared to wt Cbx2-EGFP protein. To test if such mutations could impair chromatin binding of Cbx2, we performed biochemical fractionation of protein lysates from ESCs transiently transfected with wt and mutant Cbx2-EGFP proteins (Figure 4B). Consistently, Cbx2-CD^{F12A} and Cbx2-AT^{G78R} mutants are less enriched in the chromatin fraction, and instead accumulate in nuclear soluble and cytoplasmic fractions. This effect was more pronounced for the double mutant protein arguing that Cbx2 association with chromatin requires both its CD and AT modules.

We further used NMR spectroscopy to detail the mechanism by which Cbx2 recognizes H3K27me3-marked chromatin. We investigated the binding of a short $Cbx2^{CD-AT}$ to a reconstituted recombinant nucleosome core particle modified with a methyllysine analog at H3K27 (H3Kc27me3-NCP) or a short H3K27me3 peptide (Figure 4C). $Cbx2^{CD-AT}$ was either uniformly labeled with ^{15}N (upper two panels) or specifically

labeled with ^{13}C at Ile, Leu and Val residues (lower two panels) and changes in NMR resonance frequencies (chemical shift perturbations) were measured to identify residues in Cbx2^{CD-AT} that change upon nucleosome or peptide binding. As expected, binding of a H3K27me3 peptide induced chemical shift perturbations only within the CD. Furthermore, the residues affected by peptide binding map to the known H3K27me3 binding site of Cbx2^{CD} as determined by X-ray crystallography (Kaustov et al., 2011). This indicates that in solution, the chromodomain of Cbx2^{CD-AT} binds to the H3K27me3 peptide in the same manner as the isolated CD, and there are no interactions of the AT hook domain or the linker region with the peptide. We next examined the chemical shift changes in Cbx2^{CD-AT} upon binding to the H3Kc27me3-NCP which contains two AT-rich sequences (Figure 4C, first and third panels). Again we observed expected chemical shift perturbations in the CD, although the magnitudes of the changes were weaker compared to the H3K27me3 peptide. We attribute this difference to the known lower affinity of the alkylated cysteine methyllysine analogues compared to *bona fide* trimethyllysine (Seeliger et al., 2012). Importantly, in the presence of the H3Kc27me3-NCP we observed significant changes in NMR chemical shifts in the linker between CD^{Cbx2} and AT^{Cbx2}, the AT hook itself, and in the residues immediately after AT^{Cbx2}. These data show that regions of Cbx2^{CD-AT} C-terminal to the CD are significantly involved in nucleosome binding (but not H3K27me3 binding). Furthermore, chemical shift values of the linker region when bound to H3Kc27me3-NCP are consistent with increased helical content suggesting a conformational change upon binding. Together, our NMR data are consistent with a coordinated twofold interaction of Cbx2^{CD-AT} with H3K27me3-marked nucleosomes in which CD^{Cbx2} binds the methyl mark and AT^{Cbx2} binds AT-rich regions of nucleosomal DNA.

CD^{Cbx2} directs AT^{Cbx2} binding to DNA by integrating histone modification states

We have shown that matPRC1 is excluded from mat-PCH by the *Suv39h* pathway (Puschendorf et al., 2008). Surprisingly, micro-injection of the Cbx2-CD^{F12A} construct in zygotes resulted in modest but significant accumulation of the protein as well increased H2AK119ub1 enrichment at mat-PCH compared to the Cbx2 control

construct (Figure 3B, 5A) demonstrating that functional matPRC1 complexes are targeted to these sites, regardless of the presence of H3K9me3, H4K20me3 and Hp1β. Likewise, we observed only an increased localization of Cbx2-CD^{F12A} but not of wt Cbx2 at mat-PCH in *Ezh2*$^{m-z+}$ zygotes (Figure S4A) ruling out the possibility that mat-PCH localization is driven by an increased availability of Cbx2 released from euchromatic sites. Indeed, matPRC1 components are sufficiently expressed to even bind to and modify PCH of two paternal genomes in triploid zygotes while mat-PCH is refrained from PRC1 activity (Figure 5B). Together, these data imply that a functional CD^{Cbx2} prevents AT^{Cbx2} from binding to mat-PCH.

We next investigated whether the gain of PCH localization of Cbx2-CD^{F12A} is due to the inability of the CD to read methylated histones, thereby enabling AT^{Cbx2} to bind to DNA. We transiently transfected wt ESCs with a short CD^{Cbx2}-AT^{Cbx2}-EGFP reporter construct lacking the Pc-box domain to eliminate interactions with other PRC1 components. As in zygotes, the CD^{F12A} mutation as well as another aromatic cage mutation, CD^{W33A}, enabled enrichment at PCH of wt ESCs without altering overall protein levels (Figures 5C, S4B) (Bernstein et al., 2006). Mutating additionally AT^{Cbx2} resulted in loss of PCH enrichment, confirming that the localization of CD mutants in wt cells is mediated by AT^{Cbx2}.

These results suggest that CD^{Cbx2} and AT^{Cbx2} function as one molecular unit such that the binding of AT^{Cbx2} to specific loci is determined by CD^{Cbx2} integrating the local chromatin status. This model predicts that the linker between CD^{Cbx2} and AT^{Cbx2} controls the chromatin sensing capacity of the CD-AT unit. Indeed, our NMR data (Figure 4C) supports the idea that the linker is involved in nucleosome binding. To test whether the chromatin specific targeting effect of CD^{Cbx2} is alleviated by a spatial separation of CD^{Cbx2} and AT^{Cbx2}, we replaced the 14 amino acid linker sequence by a long flexible linker consisting of 10 'TGS' repeats. We observed a similar gain in heterochromatin localization for the CD^{Cbx2}-flex-AT^{Cbx2}-EGFP as for the CD$^{Cbx2\text{-}F12A}$-AT^{Cbx2}-EGFP reporter in wt cells (Figure 5C) suggesting that the longer linker uncouples the coordinated recognition of chromatin by Cbx2$^{CD\text{-}AT}$. Indeed, introduction of the CD^{F12A} mutation in such construct (CD$^{Cbx2\text{-}F12A}$-flex-AT^{Cbx2}-EGFP) did not additionally

improve heterochromatic enrichment (Figure 5C). Intriguingly, linking CD^{Cbx2} to even more potent DNA-binding AT-hooks of the high mobility group protein HMGA1 (AT2 and AT3) reduced heterochromatic localization of such fusion protein in wt ESCs, as measured by IF and ChIP-qPCR. Inclusion of the CD^{F12A} mutation or a long flexible linker improved the localization of the EGFP reporters to chromocenters (Figure 5D-E, S4C). These results show that CD^{Cbx2} effectively reduces DNA binding of nearby high affinity AT-hooks in the context of a *Suv39h*-dependent H3K9me3-modified chromatin configuration. Moreover, the short linker sequence between CD^{Cbx2} and AT^{Cbx2} is required to sense the specific heterochromatic status for localization of PRC1.

Alanine 14 defines chromatin targeting specificity of Cbx2

Given that H3K9me3-labeled chromatin occludes Cbx2 from binding we wondered whether increasing the affinity of CD^{Cbx2} for H3K9me3 would enable Cbx2 localization at PCH in wt ESCs. Despite high conservation, CDs of *Drosophila* and mammalian Cbx and Suv39h proteins harbor several variable amino acids (Figure 6A, 6B). Comparative analysis of crystal and NMR structures of Cbx CDs revealed that most variant amino acids are not in proximity of the H3 N-terminus and may therefore not be critical for recognition of methylated H3 (Kaustov et al., 2011). An exception is residue 14 (with respect to Cbx2) which resides within a hydrophobic cavity that embraces the H3 N-tail close to the methylated lysine. This residue is an alanine in the CDs of Cbx2 and dPC which preferentially bind to H3K27me3, whereas it is a valine in CDs of Cbx4, Cbx7, HP1 proteins and the Suv39h HMTs, all recognizing H3K9me3 (Figure 6A). Interestingly, the classical EMS-induced $SU(VAR)2^{502}$ loss-of-function allele of dHP1 harbors a V-to-M substitution of this residue (Platero et al., 1995). Consistently, the corresponding mouse Hp1β V23M mutant has reduced affinity for H3K9me2 peptides (Lachner et al., 2001) and a V23A mutant fails to localize to chromocenters in wt ESCs (Figure S5A-C).

In contrast, the “inverse” A14V substitution in CD^{Cbx2} increased its affinity for H3K9me3 while leaving the affinity for H3K27me3 unaffected (Figure 6B). Consistent with representing a gain-of-function, the A14V substitution increased the PCH

localization of CD^{Cbx2}-AT^{Cbx2}- and even of CD^{dPC}-AT^{Cbx2}-EGFP reporters in wt ESCs, indicating functional conservation of the residue in Cbx2 and dPC (Figure 6C). We also observed an increased localization of full-length Cbx2-CD^{A14V} at mat-PCH compared to control showing that the A14V replacement modulates chromatin binding *in vivo* (Figure 6D). Thus, these experiments demonstrate that the exclusion of Cbx2 from mat-PCH and PCH in wt ESCs can be overcome by increasing the binding affinity of CD^{Cbx2} for H3K9me3.

Hp1β prevents PRC1 binding to mat-PCH in zygotes

The previous experiments suggest that CD^{Cbx2} effectively prevents AT^{Cbx2} from binding major satellites by competing with HP1 proteins for association with chromatin. To test this idea, we aimed at removing HP1 proteins from PCH using a genetic approach. In mouse, three dHP1 orthologs are expressed in most cell types including ESCs in which chromocenters are predominantly marked by Hp1α (Cbx5), Hp1β (Cbx1), and to a lesser extent Hp1γ (Cbx3) (Minc et al., 1999). In mouse zygotes, only Hp1β is enriched at maternal PCH in a *Suv39h2*-dependent manner correlating with H3K9me3 (Figure S6A) (Puschendorf et al., 2008). Since Hp1α and Hp1γ proteins are not present in nuclei of zygotes (Figure S6A) (Meglicki et al., 2012), we generated mice conditionally deficient for *Hp1β* during oogenesis and that would thus lack maternally provided protein during pre-implantation development. Indeed, Hp1β protein was not detectable in $Hp1\beta^{m\text{-}z+}$ zygotes (Figure 7A). Moreover, neither Hp1α nor Hp1γ were significantly up-regulated (Figure S6A), ruling out any possible compensatory mechanisms. Strikingly, all canonical matPRC1 proteins and H2AK119ub1 accumulated on mat-PCH as on pat-PCH in $Hp1\beta^{m\text{-}z+}$ zygotes (Figure 7A, S6B), as observed for $Suv39h^{m\text{-}z+}$ zygotes (Figure S6G) (Puschendorf et al., 2008). This result shows that loss of Hp1β creates a permissive state for matPRC1 binding at mat-PCH. Interestingly, we also observed an enrichment of H3K27me3 at mat-PCH in $Hp1\beta^{m\text{-}z+}$ zygotes, thereby presumably reinforcing Cbx2 binding to mat-PCH (Figure 7B). Together, these data

demonstrate that Hp1β, by binding to *Suv39h*-mediated H3K9me3, creates a chromatin state that is non-permissive for Cbx2, matPRC1 and PRC2 binding to mat-PCH.

DISCUSSION

CD^{Cbx2} and AT^{Cbx2}: two reader domains mediating cPRC1 targeting

We elucidate here the molecular mechanisms underlying targeting of PRC1 to major satellites and the control thereof by Hp1β in mouse early embryos. These mechanisms are distinct from those proposed to drive alternative heterochromatin formation by vPRC1 at PCH in *Suv39h* dn or *Dnmt* TKO ESCs (Cooper et al., 2014; Saksouk et al., 2014). We show that targeting of catalytically active matPRC1 to pat-PCH in zygotes is mediated by the CD and AT-hook of Cbx2. Mutational studies of CD^{Cbx2} and AT^{Cbx2} and competition experiments with distamycin A indicate that AT^{Cbx2} binds to AT-rich major satellites thereby targeting matPRC1 to heterochromatin in a PRC2-independent manner, as observed *in vivo* at pat-PCH following fertilization, before the acquisition of H3K27me3. Mutational studies, combined with *Ezh2* deficiency conditions, show that the interaction between CD^{Cbx2} and H3K27me3 contributes to Cbx2 association at PCH and euchromatin *in vivo*. The observed H3K27me3 selectivity is consistent with the *in vitro* binding specificity of CD^{Cbx2} (Bernstein et al., 2006; Kaustov et al., 2011). Biophysical and biochemical experiments show that both modules increase the affinity of Cbx2 for chromatin, thereby potentially controlling PRC1 targeting to specific epigenetically marked loci in the genome.

Whereas CD^{Cbx2} and AT^{Cbx2} are each sufficient for Cbx2 targeting to pat-PCH in zygotes, they contribute in an additive manner to PCH binding in ESCs. Such cell type specific binding properties may reflect possible differences in DNA accessibilities and/or H3K27me3 occupancies, resulting from dynamic changes in chromatin during the establishment versus maintenance of the repressive state in early embryos versus ESCs, respectively.

MatPRC1 members and H2AK119ub1 localize in zygotes at pat-PCH despite the presence of DNA methylation within this compartment. In contrast, we did not detect enrichment of endogenous Rybp, a common component among distinct vPRC1 complexes (Blackledge et al., 2014; Gao et al., 2012), nor of exogenous Pcgf1-EGFP, although transcripts of these and other vPRC1 members including *Kdm2b* are maternally provided to the zygote. These data support the notion that chromatin targeting of vPRC1 but not matPRC1 is inhibited by DNA methylation (Cooper et al., 2014; Saksouk et al., 2014).

Proteins or complexes bind to chromatin often via multiple reader domains that each interact with relatively low affinity to modifications on histones or DNA (Eustermann et al., 2011; Ruthenburg et al., 2011; Cheng and Blumenthal, 2010). Among Cbx proteins of the PcG family, this feature is unique to Cbx2. Others contain only a CD, which for Cbx4 and Cbx7 display moderate affinity to H3K9me3 and H3K27me3 (Figure 6B) whereas no interactions could be measured for Cbx6 or Cbx8 *in vitro* (Bernstein et al., 2006; Kaustov et al., 2011). Consistently, other PcG-Cbx proteins besides Cbx2 do not significantly bind to PCH in wt nor *Suv39h* dn ESCs (Figure S5F; data not shown). Linking AT^{Cbx2} to either CD^{Cbx4} or CD^{Cbx7}, however, resulted in targeting of chimeric reporters to PCH (Figure S5E) suggesting that the combination of CD^{Cbx4} or CD^{Cbx7} with AT^{Cbx2} provides the chimeric proteins sufficient affinity to compete with HP1 proteins for binding to PCH. Accordingly, loss of H3K9me3 affinity via a V13A mutation impaired PCH localization (Figure 6B, S5E). In zygotes, however, we observed some PCH enrichment for full length Cbx7-EGFP but not for Cbx4-EGFP whereas Cbx2-EGFP was more strongly enriched (Figure S5G). These data are consistent with previously discussed cell type specificities, differences in H3K27me3 affinities of respective CDs, the role of AT^{Cbx2} and possibly of its neighboring amino acids in binding to H3K27me3-modified nucleosomes (Figure 4C, 6B).

CD^{Cbx2} and AT^{Cbx2} functions as one molecular unit

Besides enhancing chromatin affinity, CD^{Cbx2} and AT^{Cbx2} specify together also binding selectivity. Mutating the CD or uncoupling CD^{Cbx2} and AT^{Cbx2} by increasing the

distance between these modules enabled targeting to heterochromatic sites bound by proteins of the Suv39h/HP1 pathway. We therefore propose that CD^{Cbx2} and AT^{Cbx2}, interconnected by a short linker, function as one molecular unit integrating the histone methylation and HP1 state for Cbx2 binding to chromatin. Correspondingly, *Hp1β* deficiency in zygotes allows matPRC1 localization at mat-PCH. In such embryos, H4K20me3 levels are reduced at mat-PCH, while H3K9me3 is largely unchanged (Figure S6C, D), which is consistent with Suv4-20h HMTs acting downstream of HP1 proteins (Schotta et al., 2004). Cbx2-EGFP did not localize to PCH in *Suv4-20h* dn ESCs, marked by Hp1β but lacking H4K20me3 (Figure S6E, F), indicating that Hp1β rather than H3K9me3 or any *Suv4-20h*-dependent process is inhibitory to Cbx2 binding. Whether such mechanism of steric hindrance is modulated by post-translational modifications on Cbx2 or HP1 proteins (Hatano et al., 2010), and whether it would contribute to parental specific gene repression programs during early embryogenesis remain intriguing questions.

Hp1β inhibits H3K27me3 accumulation at mat-PCH

Surprisingly, we also detected H3K27me3 enrichment at mat-PCH in $Hp1\beta^{m\text{-}z+}$ embryos despite unaltered H3K9me3 levels. These results are in accordance with reports showing co-existence of H3K9me3 and H3K27me3 at loci (Bilodeau et al., 2009) and that H3K9me3 does not inhibit PRC2 activity (Schmitges et al., 2011). They further argue that PRC2 recruitment and/or activity is negatively regulated by HP1 which may explain the exclusive localization of H3K27me3 at PCH lacking H3K9me3 in *Dnmt* TKO ESCs (Cooper et al., 2014). Although artificial tethering of a minimal Rnf2/Pcgf4 complex and resulting H2AK119ub1 are sufficient for H3K27me3 deposition at PCH, even in wt ESCs (Cooper et al., 2014), H3K27me3 localization at pat-PCH is independent of *Rnf2* function in wt zygotes and likely at mat-PCH in $Hp1\beta^{m\text{-}z+}$ embryos as well (Puschendorf et al., 2008). Hence, the function of Bend3 in H3K27me3 deposition *in vivo* awaits further investigation (Saksouk et al., 2014). If relevant, it will be important to determine to what extent Bend3 recruitment to PCH and euchromatin is controlled by Hp1β and DNA methylation reprogramming events in early embryos.

EXPERIMENTAL PROCEDURES

Constructs

Constructs for N-terminal enhanced GFP (EGFP) fusion proteins of Rnf2 and Phc2 (BD Biosciences) and 3xFlag-Bmi1 were kindly provided by Dr. Koseki. Constructs for C-terminal EGFP fusions of Cbx2, Cbx4, Cbx6, Cbx7 and Cbx8 were generously provided by Dr. Bernstein (Bernstein et al., 2006). Point mutations were generated by site-directed mutagenesis (Stratagene). *Hmga1* and *Pcgf1* were cloned by PCR from NIH3T3 and CCE cDNA respectively. For microinjection, constructs were cloned into a pcDNA3.1-poly(A) vector kindly provided by Dr. Yamagata (Yamagata et al., 2005).

Mice and Cell Lines

Ezh2$^{m\text{-}z+}$ zygotes have been reported previously (Puschendorf et al., 2008). ESC clone EPD0027_2_ H02 (EUCOMM) was used to generate *Cbx1* (Hp1β) conditionally deficient mice. Wt, *Suv39h* dn (Lehnertz et al., 2003) and *Suv4-20h* dn (Schotta et al., 2004) ESCs were transfected with fusion constructs using Lipofectamine 2000 (Invitrogen). Flow cytometry, FRAP, *in vitro* fertilization, micro-injection of CD1 or C57Bl6/J zygotes and culture of embryos is described in the Supplemental Experimental Procedures.

IF staining, Western Blot, IP and ChIP

IF staining and Western blot analysis were done as described previously (Posfai et al., 2012; Puschendorf et al., 2008; Tardat et al., 2010). Protocols and reagents for IF, image quantification, statistical analysis, protein extraction, IP, ChIP and antibodies is given in the Supplemental Experimental Procedures and Table S1.

Fluorescence Polarization and NMR

Biophysical analyses were performed as described before (Kaustov et al., 2011). Detailed information is available in the Supplemental Experimental Procedures.

ACKNOWLEDGEMENTS

We thank A. Otte, M. Vidal, H. Koseki, E. Bernstein, K. Yamagata and T. Muir for antisera and plasmids, and T. Jenuwein and G. Schotta for *Suv39h* and *Suv4-20h* dn ESCs. We are grateful to S.H. Orkin and B. Knowles for providing *Ezh2* floxed and *Zp3*-cre transgenic mice, respectively. We acknowledge excellent technical assistance by C. Kolb, F. Zilbermann, J.-F. Spetz, L. Gelman (microscopy), H. R. Hotz (bioinformatics) and E. Ozonov (expression data analysis). We thank Peters lab members for critical reading of the manuscript. Research in the Peters lab was supported by the Novartis Research Foundation, the Swiss National Science Foundation (31003A_125386 and NRP 63 - Stem Cells and Regenerative Medicine), SystemsX.ch (Cell plasticity), the Japanese Swiss Science and Technology Cooperation Program, the European Network of Excellence “The Epigenome” and the EMBO YIP program. Work in the Arrowsmith lab was funded by the Natural Sciences and Engineering Research Council of Canada, the Canadian Cancer Society and the Canadian Institutes for Health Research. M.T. was supported by the EMBO Long-Term Fellowship program. M.A. and U.B. acknowledge the Boehringer Ingelheim Fonds for their PhD fellowships.

AUTHOR CONTRIBUTIONS

M.T., M.A., R.K., L.K. C.H.A. and A.H.F.M.P. conceived and designed the experiments. M.T., M.A., R.K., Z.L., U.B., L.K. and S.D. performed the experiments. R.T. provided computational support to image analysis. M.T., M.A., R.K., L.K., C.H.A. and A.H.F.M.P. analyzed the data. M.T., R.K. and A.H.F.M.P. wrote the manuscript.

FIGURE LEGENDS

Figure 1: Cbx2-PRC1 complexes are targeted to constitutive heterochromatin in embryos and *Suv39h* dn ESCs

(A) Schematic representation of cPRC1 and vPRC1. Arrows refer to catalytic activities while dashed lines indicate binding interactions.

(B) IF of cPRC1 and vPRC1 components in wt PN5 zygotes. The cPRC1 component Phc2, the common catalytic subunit Rnf2 and H2AK119ub1 are enriched at pat-PCH (arrows). vPRC1 components Rybp and tagged Pcgf1-EGFP show no enrichment at pat-PCH.

(C) Localization of exogenously expressed matPRC1 components in nuclei of wt and *Suv39h* dn mESCs. Whereas 3xFlag-Bmi1 was detected by IF, EGFP fluorescence was directly measured. Chromocenters are brightly stained with DAPI. Quantification of protein enrichment at PCH is presented as a ratio of fluorescence intensity at PCH over euchromatin (see Figure S1F for details).

(D) IF for H2AK119ub1 and endogenous Phc1 and Rnf2 in *Suv39h* dn ESCs transiently expressing Cbx2-EGFP or EGFP alone.

(E) Localization of Cbx2-EGFP, Bmi1 and H2AK119ub1 at pat-PCH of PN5 stage zygotes (arrows) either wt or *Rnf2* deficient (*Rnf2*$^{m-z+}$). Box plots show quantification of fluorescence intensity at PCH (in arbitrary units (A.U.)).

The number of cells and embryos analyzed are shown between brackets. *p<0.05; **p≤0.01; ***p≤0.001.

Figure 2: CD^{Cbx2} and AT^{Cbx2} regulate Cbx2 targeting to PCH in *Suv39h* dn ESCs

(A) Sequence alignment of N-terminal amino acids of five mouse dPC orthologs containing chromodomains, and an AT-hook in Cbx2. Blue arrows: aromatic cage residues that enable methyl-lysine binding by CDs. Green arrows: PRGRP consensus sequence.

(B) Schematic representation of 5 mammalian PcG Cbx proteins. Chromodomains in purple, AT-hook motif in green, AT-hook like (ATL) motifs in yellow, PcBox in blue.

(C) Nuclear localization of full length Cbx2–EGFP constructs with mutations in *Suv39h* dn ESCs.

(D) Relative enrichment of Cbx2-EGFP constructs at PCH over euchromatin in *Suv39h* dn ESC nuclei.

(E) FRAP of Cbx2-, Cbx2-CD^{F12A}-, Cbx2-AT^{G78R}-EGFP was performed on chromocenters in *Suv39h* dn ESCs after transient transfection with indicated constructs (the bleached region is indicated by a white arrow, top panel). Recovery kinetics were measured over a period of 60 sec (lower panel). The estimated recovery half-times are 8.72 ± 5.06s, 2.26 ± 1.12s and 2.13 ± 1.01s for Cbx2-, Cbx2-CD^{F12A}- and Cbx2-^{G78R}-EGFP respectively (values represent mean ± SD; n = ~25 per construct).

(F) Enrichment of Cbx2-EGFP constructs at PCH in *Suv39h* dn ESCs as measured by ChIP-qPCR analysis of mouse major satellite repeats. Data are represented as percent of input chromatin. Error bars represent SD.

Figure 3: Cbx2 targeting to hetero- and euchromatin in zygotes.

(A) IF images (left panel) and quantification of Cbx2 and Rnf2 fluorescence signal at PCH of decondensing sperm heads in PN0 stage zygotes, untreated (control) or treated with 20µM and 50µM distamycin A.

(B) Localization of Cbx2-EGFP constructs at PCH of maternal and paternal pronuclei of PN5 stage one-cell embryos (arrows, left panel). Box plots show quantification of EGFP fluorescence intensity at mat-PCH, pat-PCH and euchromatin for each construct

(C) Localization of Cbx2 and Cbx2-AT^{G78R} EGFP constructs in paternal PCH and euchromatin of wt and *Ezh2*$^{m-z+}$ zygotes (left panel). Box plots show quantification of EGFP and H3K27me3 fluorescence intensity at mat-PCH and euchromatin for each construct.

The number of embryos analyzed is shown between brackets. *p<0.05; ***p≤0.001; ns: not significant.

Figure 4: CD^{Cbx2} and AT^{Cbx2} control chromatin binding.

(A) Co-IP of Cbx2 with H3K27me3-modified nucleosomes. Whole-cell extracts from HEK293 cells expressing Cbx2-EGFP constructs were IP-ed with anti-EGFP antibody and analyzed by immunoblot with indicated antibodies.

(B) Sub-cellular distribution of Cbx2-EGFP proteins in ESCs. β-Tubulin and Lamin A/C were used as controls for cytoplasmic and chromatin fractions.

(C) Structural basis for Cbx2 interaction with the nucleosome. $Cbx2^{CD-AT}$ complexes with methyllysine analog H3Kc27me3-NCP and H3K27me3 peptide (residues 19-33) were prepared by titrating aliquots of nucleosome or peptide into the indicated isotope-labeled protein. Top panels: ^{1}H-^{15}N chemical shift perturbations (CSP) for $Cbx2^{CD-AT}$ (residues 9-88) *vs* residue number when bound to either a recombinant modified nucleosome core particle H3Kc27me3-NCP (1:2 (blue) and 1:3 (maroon) molar ratios, Cbx2:nucleosome) or a synthetic H3K27me3 peptide (1:1 (light blue), 1:3 (pink) and 1:6 (maroon) molar ratios, Cbx2:peptide, second panel). Open circles indicate either unassigned peaks or peaks that can not be observed in the [^{1}H,^{15}N]-TROSY spectrum before titration. Solid black circles correspond to Prolines which do not have peaks. Red circles indicate peaks that disappear upon binding. Bottom panels: CSP weighted average of the [^{1}H,^{13}C] methyl chemical shift changes of $Cbx2^{CD-AT}$ with Ile, Leu and Val residues selectively ^{13}C-labeled and titrated with the H3Kc27me3 nucleosome (1:1 (blue), 1:2 (light blue) and 1:3 (dark blue) molar ratios, Cbx2:nucleosome) or to the synthetic H3K27me3 peptide (1:3 (blue) and 1:6 (maroon) molar ratios, Cbx2:peptide). CSP were calculated using the equation $\Delta(\delta^{1}H\text{-}^{15}N) = [(\Delta\delta^{1}H)2 + (\Delta\delta^{15}N/5)2]1/2$ and $\Delta(\delta^{1}H\text{-}^{13}C) = [(\Delta\delta^{1}H)2 + (\Delta\delta^{13}C/4)2]1/2$, respectively.

Figure 5: CD^{Cbx2} regulates DNA binding of AT^{Cbx2} by integrating histone modification states.

(A) Localization of Cbx2- and Cbx2-CD^{F12A}-EGFP constructs and H2AK119ub1 staining at PCH of maternal pronuclei of PN5 stage zygotes (arrows). Box plots showing quantification of EGFP and H2AK119ub1 fluorescence intensity at mat-PCH for each indicated construct.

(B) IF of Rnf2 and H2AK119ub1 at pat-PCH of two paternal genomes in triploid mouse zygotes.

(C) Schematic representation of Cbx2-EGFP short reporter constructs and quantification of their PCH enrichment in wt ESCs.

(D) Schematic representation of CD^{Cbx2} and AT^{Hmga1} fusion proteins. Box plots represent quantification of EGFP signal on PCH relative to euchromatin for the indicated EGFP tagged constructs.

(E) Histogram for EGFP ChIP-qPCR analysis of mouse major satellites in wt ESCs upon transient transfection with indicated CD^{Cbx2}-AT^{Hmga1} fusion proteins. Data are represented as percent of input chromatin. Error bars represent SD.

Asterisks refer to inserted point mutations. The number of embryos or cells analyzed are shown between brackets. *$p<0.05$; ***$p\leq0.001$.

Figure 6: Alanine 14 defines chromatin targeting specificity of Cbx2.

(A) Sequence alignment of the CDs of dPC, dHP1 and their murine orthologs, and of the mouse Suv39h HMTs.

(B) Dissociation constant (K_d) values for mutant and control CDs of Cbx proteins with methylated peptides. K_ds were designated as >500µM when interactions were too weak to determine the K_d. Control values are from Kaustov et al. (2011).

(C) EGFP images and quantification of PCH enrichment of chimeric EGFP reporters containing the CD of Cbx2 or dPC fused to AT^{Cbx2} with or without the A14V mutation.

(D) EGFP images and quantification of EGFP fluorescence intensity at mat-PCH and pat-PCH for the indicated constructs in wt zygotes.

The numbers of embryos analyzed are shown between brackets. ***p≤0.001; ns: not significant.

Figure 7: Hp1β prevents PRC1 binding to mat-PCH in zygotes.

(A) IF showing enrichment of matPRC1 components Cbx2, Rnf2, and H2AK119ub1 at mat-PCH in *Hp1β*$^{m-z+}$ zygotes but not in wt PN5 zygotes (arrows). Box plots show quantification of fluorescence intensity for indicated antibodies at mat-PCH and pat-PCH in wt and *Hp1β*$^{m-z+}$ zygotes.

(B) IF analysis showing increased levels of H3K27me3 at mat-PCH (arrows). Box plot shows quantification of fluorescence intensity of H3K27me3 at mat-PCH in wt and *Hp1β*$^{m-z+}$ zygotes.

(C) matPRC1 is targeted to pat-PCH in zygotes by CD^{Cbx2} binding to *Ezh2*-mediated H3K27me3 and AT^{Cbx2} binding to DNA (presumably to major satellites). At mat-PCH, Cbx2 binding is prevented by maternally provided Hp1β bound to H3K9me3 via its CD. PRC2 targeting and/or activity is also inhibited by Hp1β.

The number of embryos analyzed is shown between brackets. **p≤0.01; ***p≤0.001; ns: not significant.

REFERENCES

Albert, M., and Peters, A.H.F.M. (2009). Genetic and epigenetic control of early mouse development. Curr. Opin. Genet. Dev. *19*, 113–121.

Aloia, L., Di Stefano, B., and Di Croce, L. (2013). Polycomb complexes in stem cells and embryonic development. Dev. Camb. Engl. *140*, 2525–2534.

Arand, J., Wossidlo, M., Lepikhov, K., Peat, J.R., Reik, W., and Walter, J. (2015). Selective impairment of methylation maintenance is the major cause of DNA methylation reprogramming in the early embryo. Epigenetics Chromatin *8*, 1.

Beisel, C., and Paro, R. (2011). Silencing chromatin: comparing modes and mechanisms. Nat. Rev. Genet. *12*, 123–135.

Bernstein, E., Duncan, E.M., Masui, O., Gil, J., Heard, E., and Allis, C.D. (2006). Mouse polycomb proteins bind differentially to methylated histone H3 and RNA and are enriched in facultative heterochromatin. Mol. Cell. Biol. *26*, 2560–2569.

Bilodeau, S., Kagey, M.H., Frampton, G.M., Rahl, P.B., and Young, R.A. (2009). SetDB1 contributes to repression of genes encoding developmental regulators and maintenance of ES cell state. Genes Dev. *23*, 2484–2489.

Blackledge, N.P., Farcas, A.M., Kondo, T., King, H.W., McGouran, J.F., Hanssen, L.L.P., Ito, S., Cooper, S., Kondo, K., Koseki, Y., et al. (2014). Variant PRC1 Complex-Dependent H2A Ubiquitylation Drives PRC2 Recruitment and Polycomb Domain Formation. Cell.

Campos, E.I., and Reinberg, D. (2009). Histones: annotating chromatin. Annu. Rev. Genet. *43*, 559–599.

Cao, R., Wang, L., Wang, H., Xia, L., Erdjument-Bromage, H., Tempst, P., Jones, R.S., and Zhang, Y. (2002). Role of histone H3 lysine 27 methylation in Polycomb-group silencing. Science *298*, 1039–1043.

Cheng, X., and Blumenthal, R.M. (2010). Coordinated chromatin control: structural and functional linkage of DNA and histone methylation. Biochemistry (Mosc.) *49*, 2999–3008.

Cooper, S., Dienstbier, M., Hassan, R., Schermelleh, L., Sharif, J., Blackledge, N.P., De Marco, V., Elderkin, S., Koseki, H., Klose, R., et al. (2014). Targeting Polycomb to Pericentric Heterochromatin in Embryonic Stem Cells Reveals a Role for H2AK119u1 in PRC2 Recruitment. Cell Rep.

Eustermann, S., Yang, J.-C., Law, M.J., Amos, R., Chapman, L.M., Jelinska, C., Garrick, D., Clynes, D., Gibbons, R.J., Rhodes, D., et al. (2011). Combinatorial readout of histone H3 modifications specifies localization of ATRX to heterochromatin. Nat. Struct. Mol. Biol. *18*, 777–782.

Fodor, B.D., Shukeir, N., Reuter, G., and Jenuwein, T. (2010). Mammalian Su(var) genes in chromatin control. Annu. Rev. Cell Dev. Biol. *26*, 471–501.

Gao, Z., Zhang, J., Bonasio, R., Strino, F., Sawai, A., Parisi, F., Kluger, Y., and Reinberg, D. (2012). PCGF Homologs, CBX Proteins, and RYBP Define Functionally Distinct PRC1 Family Complexes. Mol. Cell *45*, 344–356.

García, E., Marcos-Gutiérrez, C., del Mar Lorente, M., Moreno, J.C., and Vidal, M. (1999). RYBP, a new repressor protein that interacts with components of the mammalian Polycomb complex, and with the transcription factor YY1. EMBO J. *18*, 3404–3418.

Gill, M.E., Erkek, S., and Peters, A.H.F.M. (2012). Parental epigenetic control of embryogenesis: a balance between inheritance and reprogramming? Curr. Opin. Cell Biol. *24*, 387–396.

Guenatri, M., Bailly, D., Maison, C., and Almouzni, G. (2004). Mouse centric and pericentric satellite repeats form distinct functional heterochromatin. J. Cell Biol. *166*, 493–505.

Hahn, M., Dambacher, S., Dulev, S., Kuznetsova, A.Y., Eck, S., Wörz, S., Sadic, D., Schulte, M., Mallm, J.-P., Maiser, A., et al. (2013). Suv4-20h2 mediates chromatin compaction and is important for cohesin recruitment to heterochromatin. Genes Dev. *27*, 859–872.

Hatano, A., Matsumoto, M., Higashinakagawa, T., and Nakayama, K.I. (2010). Phosphorylation of the chromodomain changes the binding specificity of Cbx2 for methylated histone H3. Biochem. Biophys. Res. Commun. *397*, 93–99.

Inoue, A., Shen, L., Dai, Q., He, C., and Zhang, Y. (2011). Generation and replication-dependent dilution of 5fC and 5caC during mouse preimplantation development. Cell Res. *21*, 1670–1676.

Kalb, R., Latwiel, S., Baymaz, H.I., Jansen, P.W.T.C., Müller, C.W., Vermeulen, M., and Müller, J. (2014). Histone H2A monoubiquitination promotes histone H3 methylation in Polycomb repression. Nat. Struct. Mol. Biol.

Kaustov, L., Ouyang, H., Amaya, M., Lemak, A., Nady, N., Duan, S., Wasney, G.A., Li, Z., Vedadi, M., Schapira, M., et al. (2011). Recognition and specificity determinants of the human cbx chromodomains. J. Biol. Chem. *286*, 521–529.

Lachner, M., O'Carroll, D., Rea, S., Mechtler, K., and Jenuwein, T. (2001). Methylation of histone H3 lysine 9 creates a binding site for HP1 proteins. Nature *410*, 116–120.

Lehnertz, B., Ueda, Y., Derijck, A.A.H.A., Braunschweig, U., Perez-Burgos, L., Kubicek, S., Chen, T., Li, E., Jenuwein, T., and Peters, A.H.F.M. (2003). Suv39h-mediated histone H3 lysine 9 methylation directs DNA methylation to major satellite repeats at pericentric heterochromatin. Curr. Biol. CB *13*, 1192–1200.

Li, E., Bestor, T.H., and Jaenisch, R. (1992). Targeted mutation of the DNA methyltransferase gene results in embryonic lethality. Cell *69*, 915–926.

Meglicki, M., Teperek-Tkacz, M., and Borsuk, E. (2012). Appearance and heterochromatin localization of HP1α in early mouse embryos depends on cytoplasmic clock and H3S10 phosphorylation. Cell Cycle Georget. Tex *11*, 2189–2205.

Minc, E., Allory, Y., Worman, H.J., Courvalin, J.C., and Buendia, B. (1999). Localization and phosphorylation of HP1 proteins during the cell cycle in mammalian cells. Chromosoma *108*, 220–234.

Park, S.-J., Komata, M., Inoue, F., Yamada, K., Nakai, K., Ohsugi, M., and Shirahige, K. (2013). Inferring the choreography of parental genomes during fertilization from ultralarge-scale whole-transcriptome analysis. Genes Dev. *27*, 2736–2748.

Peters, A.H., O'Carroll, D., Scherthan, H., Mechtler, K., Sauer, S., Schöfer, C., Weipoltshammer, K., Pagani, M., Lachner, M., Kohlmaier, A., et al. (2001). Loss of the Suv39h histone methyltransferases impairs mammalian heterochromatin and genome stability. Cell *107*, 323–337.

Peters, A.H.F.M., Kubicek, S., Mechtler, K., O'Sullivan, R.J., Derijck, A.A.H.A., Perez-Burgos, L., Kohlmaier, A., Opravil, S., Tachibana, M., Shinkai, Y., et al. (2003). Partitioning and plasticity of repressive histone methylation states in mammalian chromatin. Mol. Cell *12*, 1577–1589.

Platero, J.S., Hartnett, T., and Eissenberg, J.C. (1995). Functional analysis of the chromo domain of HP1. EMBO J. *14*, 3977–3986.

Posfai, E., Kunzmann, R., Brochard, V., Salvaing, J., Cabuy, E., Roloff, T.C., Liu, Z., Tardat, M., van Lohuizen, M., Vidal, M., et al. (2012). Polycomb function during oogenesis is required for mouse embryonic development. Genes Dev. *26*, 920–932.

Puschendorf, M., Terranova, R., Boutsma, E., Mao, X., Isono, K., Brykczynska, U., Kolb, C., Otte, A.P., Koseki, H., Orkin, S.H., et al. (2008). PRC1 and Suv39h specify parental asymmetry at constitutive heterochromatin in early mouse embryos. Nat. Genet. *40*, 411–420.

Radic, M.Z., Saghbini, M., Elton, T.S., Reeves, R., and Hamkalo, B.A. (1992). Hoechst 33258, distamycin A, and high mobility group protein I (HMG-I) compete for binding to mouse satellite DNA. Chromosoma *101*, 602–608.

Reeves, R., and Nissen, M.S. (1990). The A.T-DNA-binding domain of mammalian high mobility group I chromosomal proteins. A novel peptide motif for recognizing DNA structure. J. Biol. Chem. *265*, 8573–8582.

Ruthenburg, A.J., Li, H., Milne, T.A., Dewell, S., McGinty, R.K., Yuen, M., Ueberheide, B., Dou, Y., Muir, T.W., Patel, D.J., et al. (2011). Recognition of a mononucleosomal histone modification pattern by BPTF via multivalent interactions. Cell *145*, 692–706.

Saksouk, N., Barth, T.K., Ziegler-Birling, C., Olova, N., Nowak, A., Rey, E., Mateos-Langerak, J., Urbach, S., Reik, W., Torres-Padilla, M.-E., et al. (2014). Redundant Mechanisms to Form Silent Chromatin at Pericentromeric Regions Rely on BEND3 and DNA Methylation. Mol. Cell *56*, 580–594.

Santos, F., Peters, A.H., Otte, A.P., Reik, W., and Dean, W. (2005). Dynamic chromatin modifications characterise the first cell cycle in mouse embryos. Dev. Biol. *280*, 225–236.

Schmitges, F.W., Prusty, A.B., Faty, M., Stützer, A., Lingaraju, G.M., Aiwazian, J., Sack, R., Hess, D., Li, L., Zhou, S., et al. (2011). Histone Methylation by PRC2 Is Inhibited by Active Chromatin Marks. Mol. Cell *42*, 330–341.

Schotta, G., Lachner, M., Sarma, K., Ebert, A., Sengupta, R., Reuter, G., Reinberg, D., and Jenuwein, T. (2004). A silencing pathway to induce H3-K9 and H4-K20 trimethylation at constitutive heterochromatin. Genes Dev. *18*, 1251–1262.

Seeliger, D., Soeroes, S., Klingberg, R., Schwarzer, D., Grubmüller, H., and Fischle, W. (2012). Quantitative assessment of protein interaction with methyl-lysine analogues by hybrid computational and experimental approaches. ACS Chem. Biol. *7*, 150–154.

Tardat, M., Brustel, J., Kirsh, O., Lefevbre, C., Callanan, M., Sardet, C., and Julien, E. (2010). The histone H4 Lys 20 methyltransferase PR-Set7 regulates replication origins in mammalian cells. Nat. Cell Biol.

Vissel, B., and Choo, K.H. (1989). Mouse major (gamma) satellite DNA is highly conserved and organized into extremely long tandem arrays: implications for recombination between nonhomologous chromosomes. Genomics *5*, 407–414.

Yamagata, K., Yamazaki, T., Yamashita, M., Hara, Y., Ogonuki, N., and Ogura, A. (2005). Noninvasive visualization of molecular events in the mammalian zygote. Genes. N. Y. N 2000 *43*, 71–79.

Yokobayashi, S., Liang, C.-Y., Kohler, H., Nestorov, P., Liu, Z., Vidal, M., van Lohuizen, M., Roloff, T.C., and Peters, A.H.F.M. (2013). PRC1 coordinates timing of sexual differentiation of female primordial germ cells. Nature *495*, 236–240.

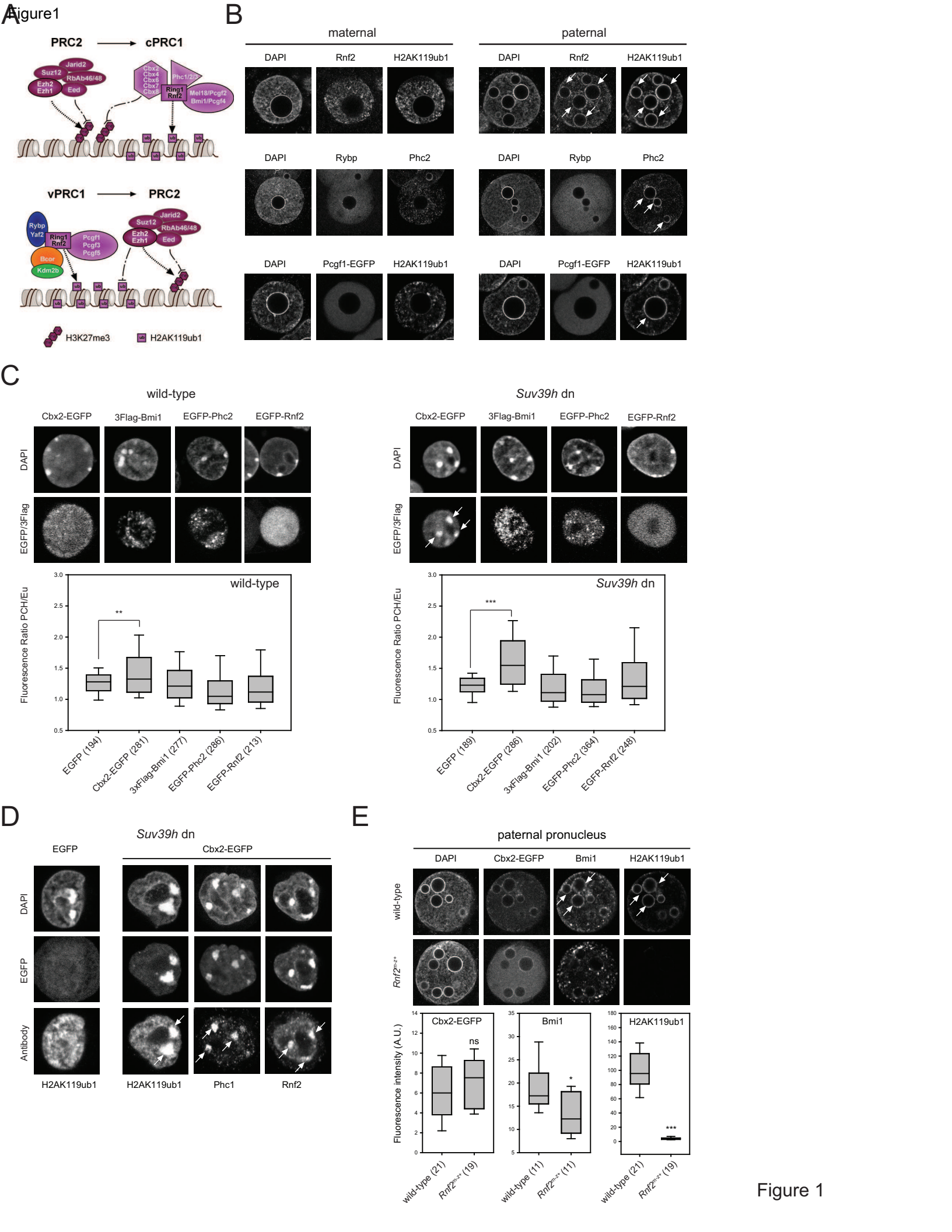
A
PRC2
cPRC1
Jarid2
Suz12
RbAb46/48
Ezh2
Ezh1
Eed
Cbx2
Cbx4
Cbx6
Cbx7
Cbx8
Phc1/2/3
Ring1
Rnf2
Mel18/Pcgf2
Bmi1/Pcgf4
vPRC1
PRC2
Rybp
Yaf2
Ring1
Rnf2
Pcgf1
Pcgf3
Pcgf5
Bcor
Kdm2b
Jarid2
Suz12
RbAb46/48
Ezh2
Ezh1
Eed
H3K27me3
H2AK119ub1
B
maternal
paternal
DAPI
Rnf2
H2AK119ub1
DAPI
Rybp
Phc2
DAPI
Pcgf1-EGFP
H2AK119ub1
C
wild-type
Suv39h dn
Cbx2-EGFP
3Flag-Bmi1
EGFP-Phc2
EGFP-Rnf2
DAPI
EGFP/3Flag
Fluorescence Ratio PCH/Eu
wild-type
Suv39h dn
**
***
EGFP (194)
Cbx2-EGFP (281)
3xFlag-Bmi1 (277)
EGFP-Phc2 (286)
EGFP-Rnf2 (213)
EGFP (189)
Cbx2-EGFP (286)
3xFlag-Bmi1 (202)
EGFP-Phc2 (364)
EGFP-Rnf2 (248)
D
Suv39h dn
EGFP
Cbx2-EGFP
DAPI
EGFP
Antibody
H2AK119ub1
H2AK119ub1
Phc1
Rnf2
E
paternal pronucleus
DAPI
Cbx2-EGFP
Bmi1
H2AK119ub1
wild-type
Rnf2mz+
Fluorescence intensity (A.U.)
Cbx2-EGFP
Bmi1
H2AK119ub1
ns
*
***
wild-type (21)
Rnf2mz+ (19)
wild-type (11)
Rnf2mz+ (11)
wild-type (21)
Rnf2mz+ (19)

Figure 1

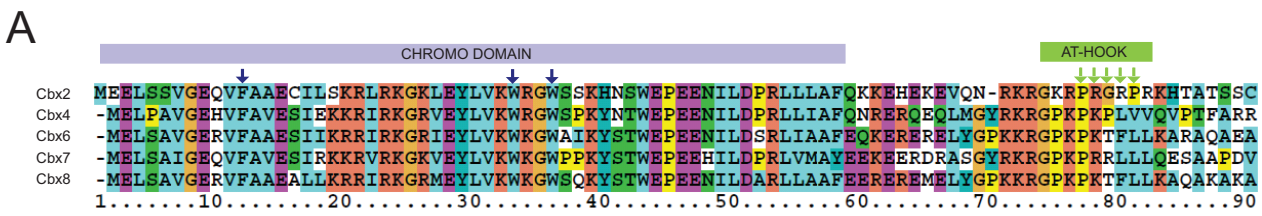
A
CHROMO DOMAIN
AT-HOOK
Cbx2 MEELSSVGEQVFAAECILSKRLRKGKLEYLVKWRGWSSKHNSWEPEENILDPRLLLAFQKKEHEKEVQN-RKRGKRPRGRPRKHTATSSC
Cbx4 -MELPAVGEHVFAVESIEKKRIRKGRVEYLVKWRGWSPKYNTWEPEENILDPRLLIAFQNRERQEQLMGYRKRGPKPKPLVVQVPTFARR
Cbx6 -MELSAVGERVFAAESIIKRRIRKGRIEYLVKWKGWAIKYSTWEPEENILDSRLIAAFEQKERERELYGPKKRGPKPKTFLLKARAQAEA
Cbx7 -MELSAIGEQVFAVESIRKKRVRKGKVEYLVKWKGWPPKYSTWEPEEHILDPRLVMAYEEKEERDRASGYRKRGPKPRRLLLQESAAPDV
Cbx8 -MELSAVGERVFAAEALLKRRIRKGRMEYLVKWKGWSQKYSTWEPEENILDARLLAAFEERERERMELYGPKKRGPKPKTFLLKAQAKAKA
1.....10.....20.....30.....40.....50.....60.....70.....80.....90

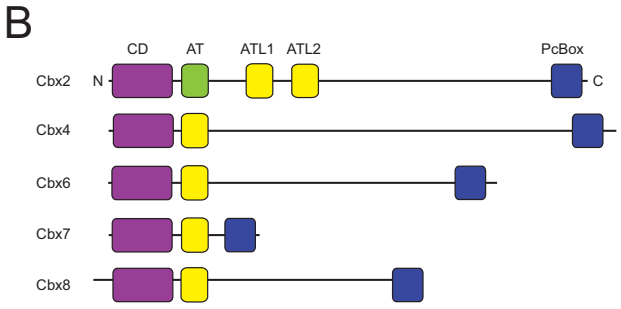
B
CD
AT
ATL1
ATL2
PcBox
Cbx2
N
C
Cbx4
Cbx6
Cbx7
Cbx8

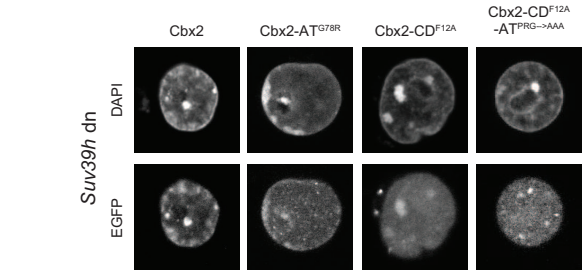
C
Cbx2
Cbx2-AT^G78R
Cbx2-CD^F12A
Cbx2-CD^F12A -AT^PRG->AAA
Suv39h dn
DAPI
EGFP

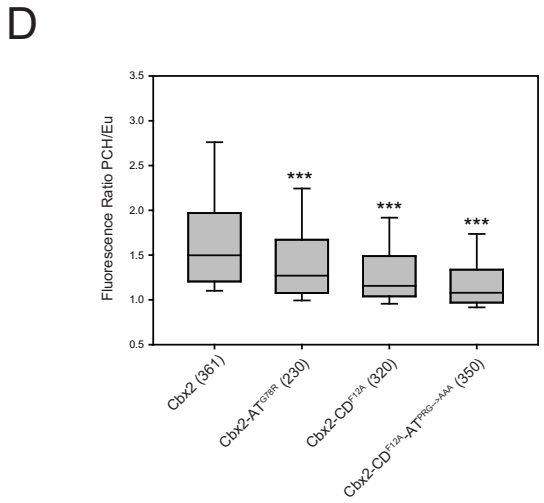
D
Fluorescence Ratio PCH/Eu
3.5
3.0
2.5
2.0
1.5
1.0
0.5
***
***
***
Cbx2 (361)
Cbx2-AT^G78R (230)
Cbx2-CD^F12A (320)
Cbx2-CD^F12A-AT^PRG->AAA (350)

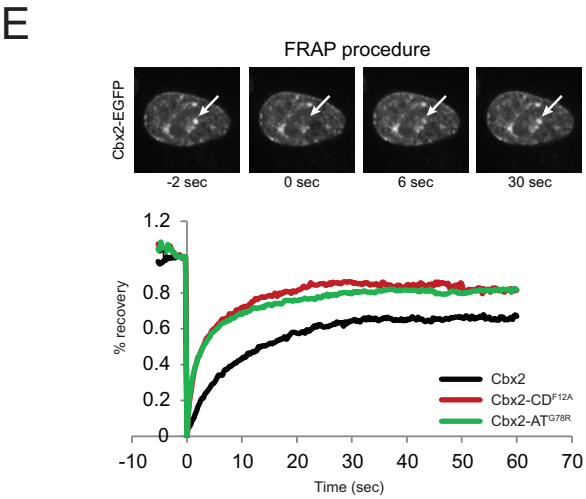
E
FRAP procedure
Cbx2-EGFP
-2 sec
0 sec
6 sec
30 sec
% recovery
1.2
0.8
0.6
0.4
0.2
0
-10
0
10
20
30
40
50
60
70
Time (sec)
Cbx2
Cbx2-CD^F12A
Cbx2-AT^G78R

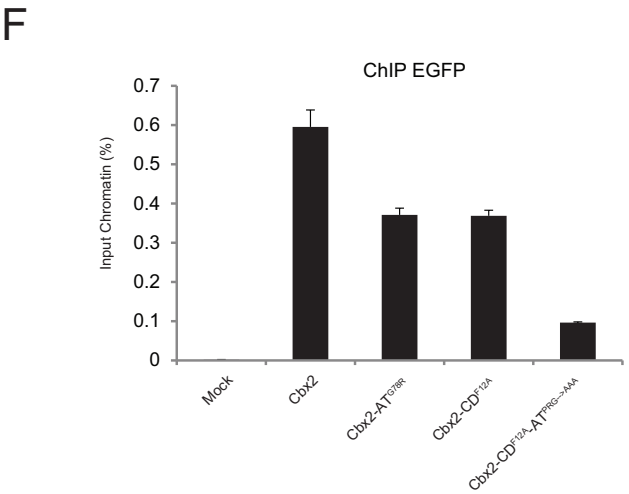
F
ChIP EGFP
Input Chromatin (%)
0.7
0.6
0.5
0.4
0.3
0.2
0.1
0
Mock
Cbx2
Cbx2-AT^G78R
Cbx2-CD^F12A
Cbx2-CD^F12A-AT^PRG->AAA

Figure3

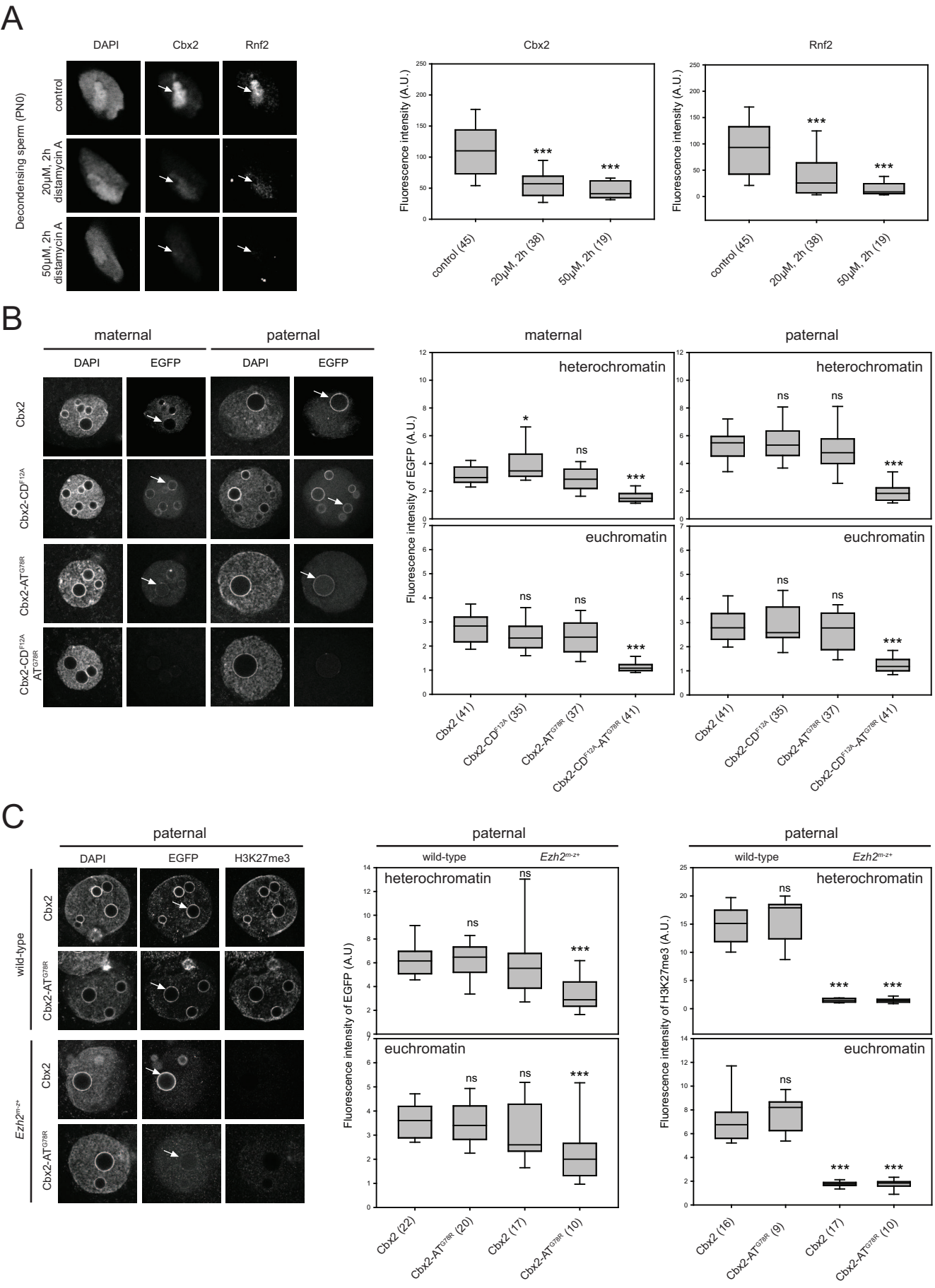

Figure 3

Figure4

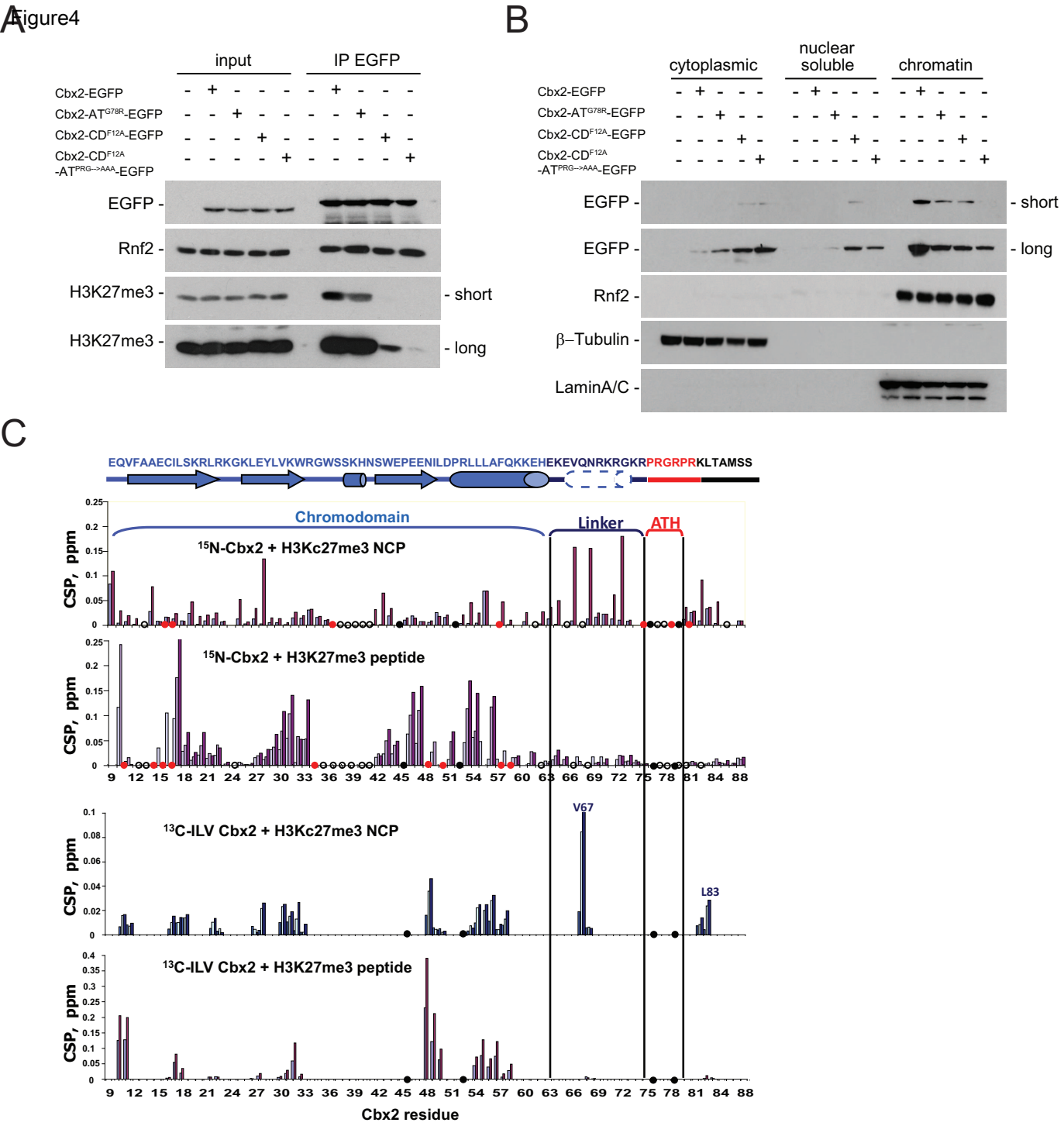

C

Figure 4

Figure5

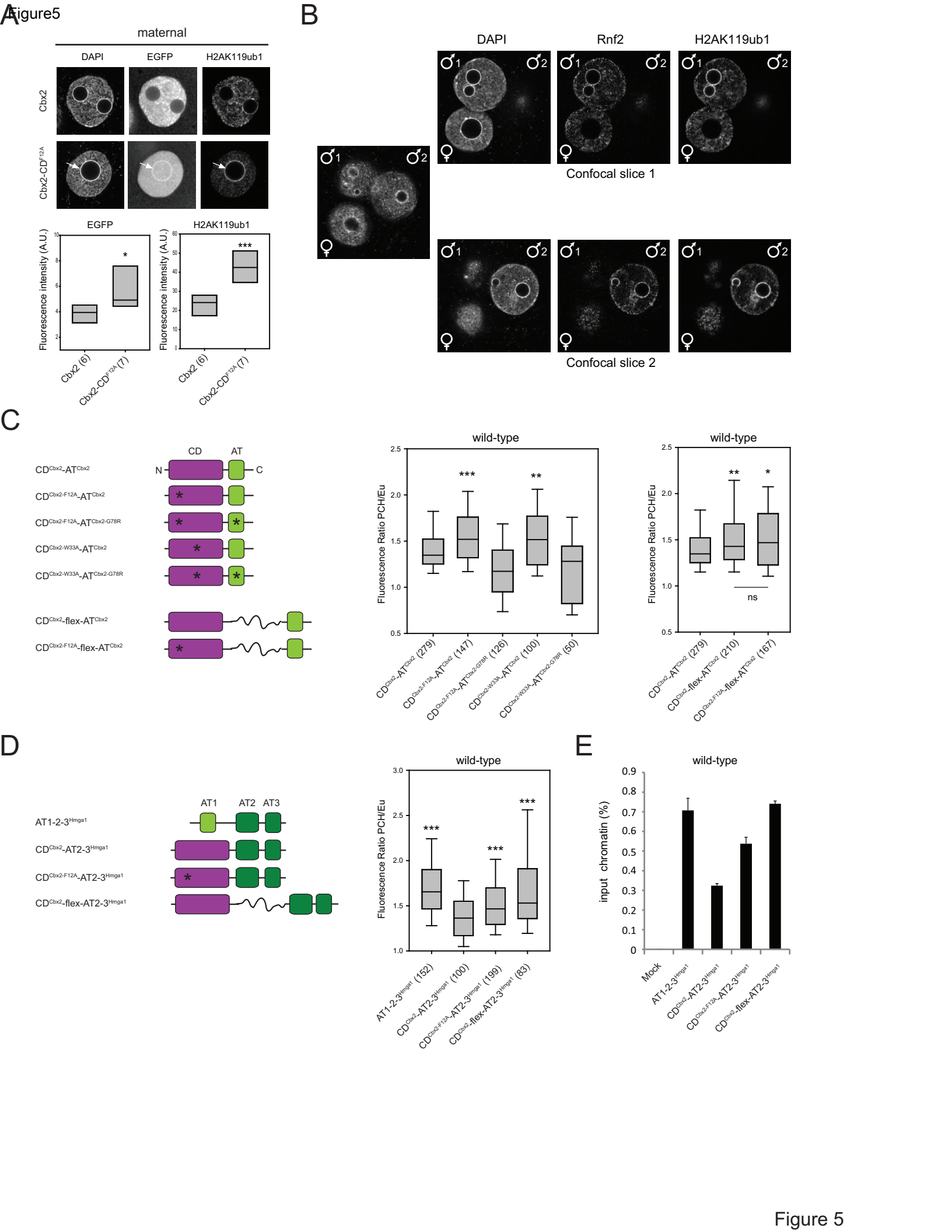

Figure 5

A

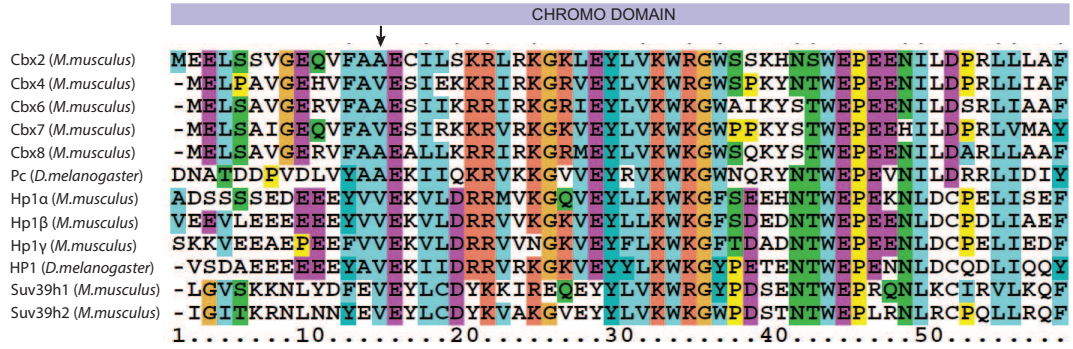

B

Protein (CD)	$K_{d\ peptide}$ (μM)	
	H3K9me3	H3K27me3
Cbx2	> 500	185 ± 20
Cbx2^{A14V}	275 ± 25	180 ± 15
Cbx4	70 ± 7	205 ± 20
Cbx4^{V13A}	> 500	395 ± 50
Cbx7	55 ± 5	110 ±17
Cbx7^{V13A}	> 500	> 500

C

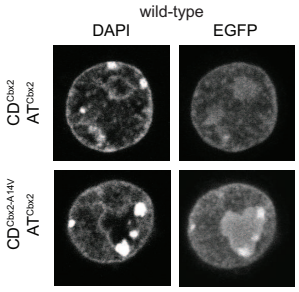

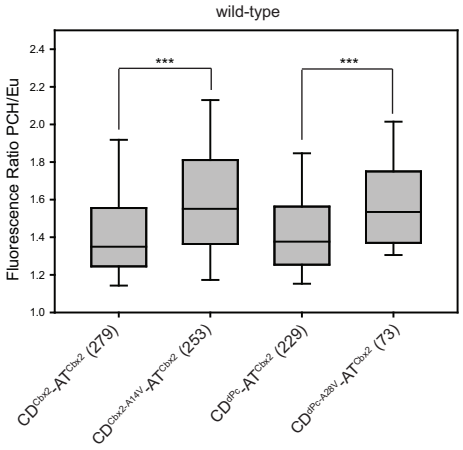

D

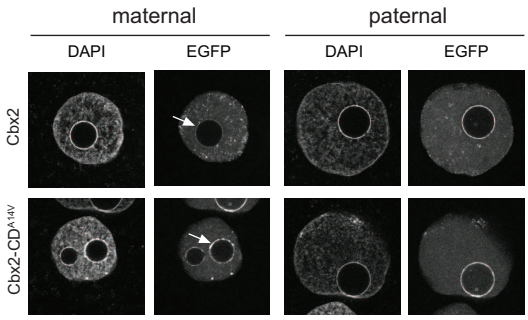

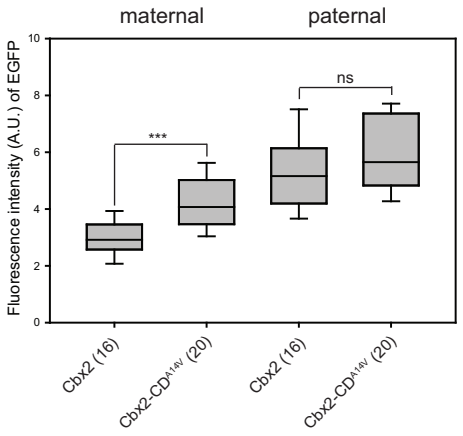

A

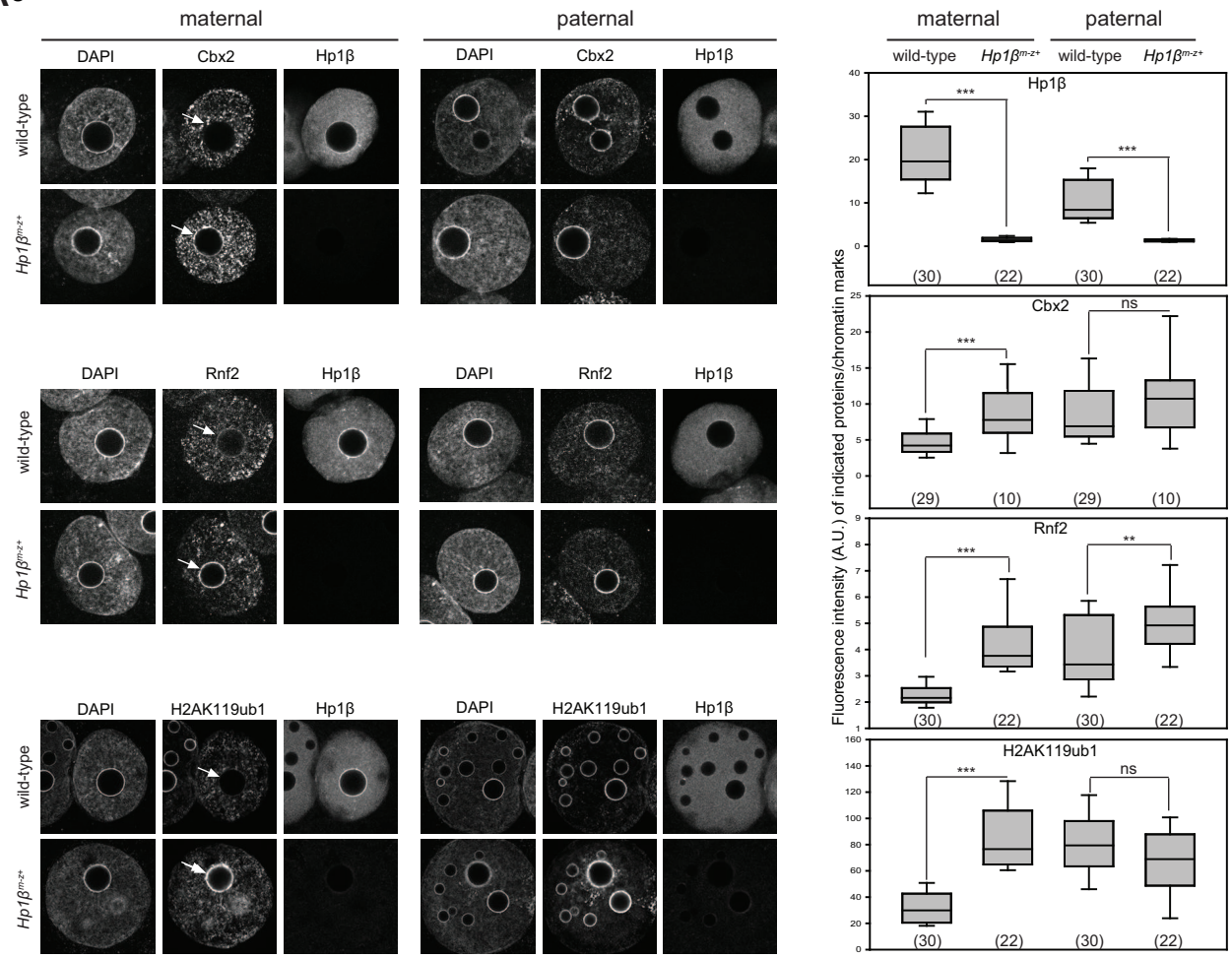
maternal
paternal
DAPI
Cbx2
Hp1β
Rnf2
H2AK119ub1
wild-type
Hp1β^m-z+
wild-type
Hp1β^m-z+
Hp1β
Cbx2
Rnf2
H2AK119ub1
Fluorescence intensity (A.U.) of indicated proteins/chromatin marks
***
**
ns
(30)
(22)
(29)
(10)

B

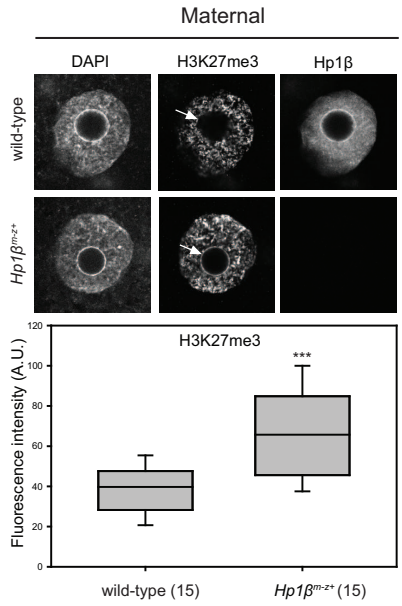
Maternal
DAPI
H3K27me3
Hp1β
wild-type
Hp1β^m-z+
H3K27me3
Fluorescence intensity (A.U.)
***
wild-type (15)
Hp1β^m-z+ (15)

C

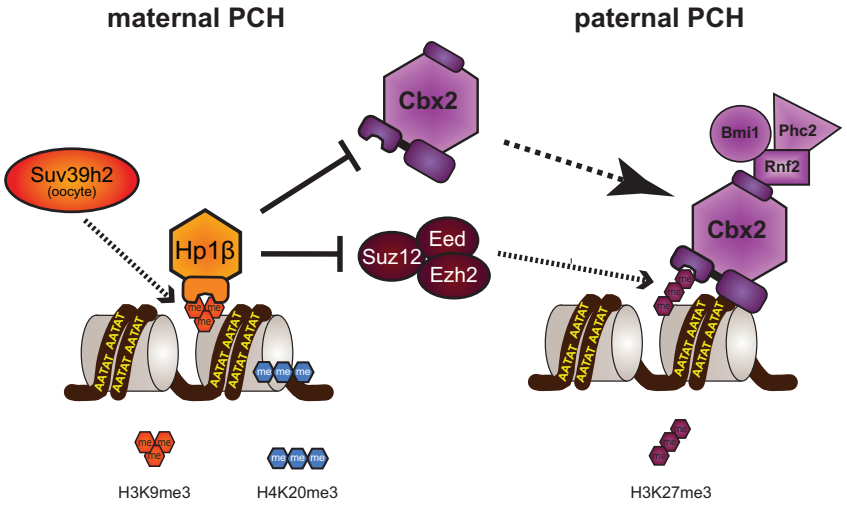
maternal PCH
paternal PCH
Suv39h2
(oocyte)
Hp1β
Cbx2
Suz12
Eed
Ezh2
Bmi1
Phc2
Rnf2
H3K9me3
H4K20me3
H3K27me3

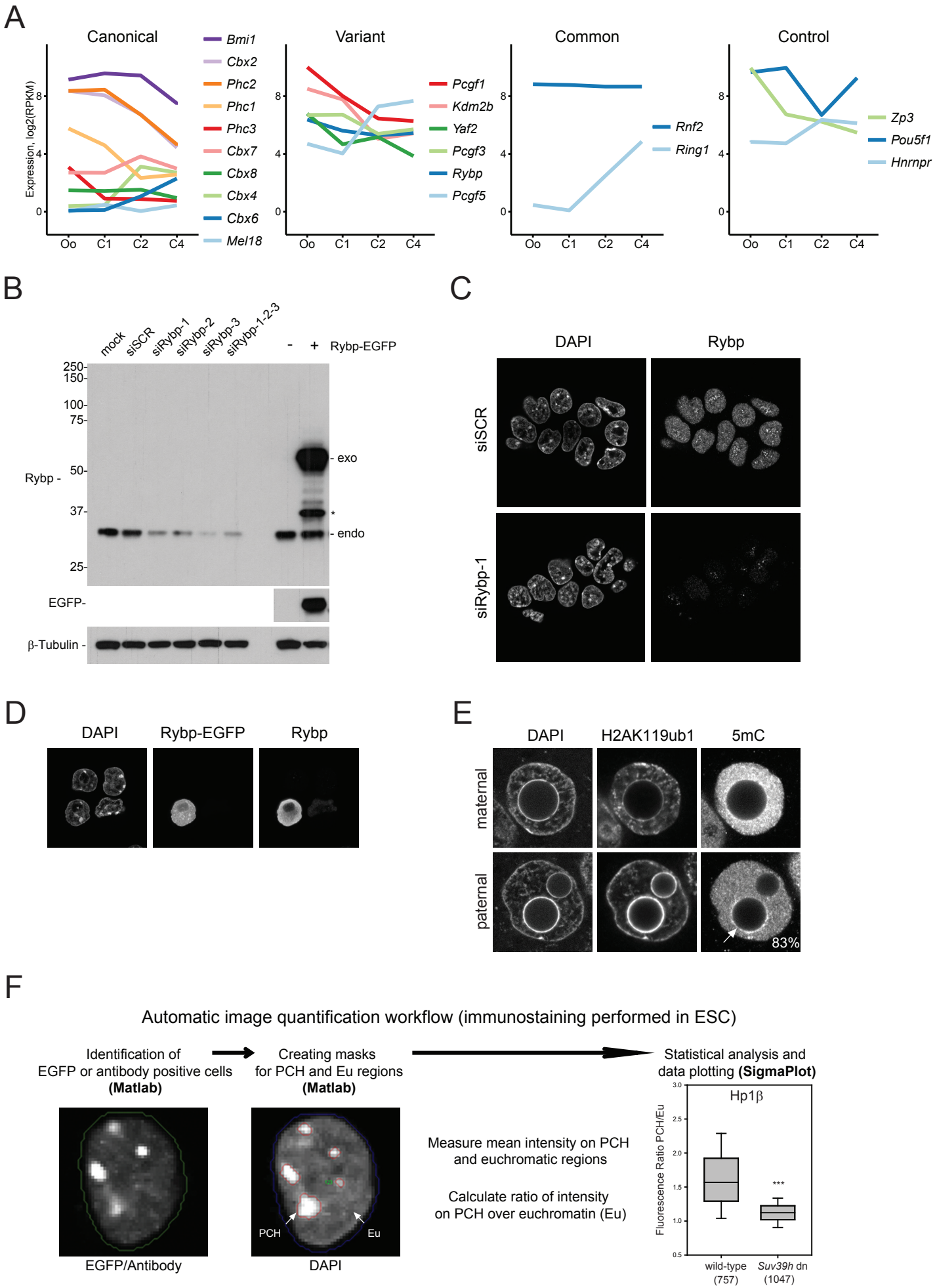
A
Canonical
Variant
Common
Control
Expression, log2(RPKM)
Oo
C1
C2
C4
Bmi1
Cbx2
Phc2
Phc1
Phc3
Cbx7
Cbx8
Cbx4
Cbx6
Mel18
Pcgf1
Kdm2b
Yaf2
Pcgf3
Rybp
Pcgf5
Rnf2
Ring1
Zp3
Pou5f1
Hnrnpr
B
mock
siSCR
siRybp-1
siRybp-2
siRybp-3
siRybp-1-2-3
- + Rybp-EGFP
250
150
100
75
50
37
25
Rybp -
- exo
*
- endo
EGFP-
β-Tubulin -
C
DAPI
Rybp
siSCR
siRybp-1
D
DAPI
Rybp-EGFP
Rybp
E
DAPI
H2AK119ub1
5mC
maternal
paternal
83%
F
Automatic image quantification workflow (immunostaining performed in ESC)
Identification of EGFP or antibody positive cells (Matlab)
Creating masks for PCH and Eu regions (Matlab)
Statistical analysis and data plotting (SigmaPlot)
EGFP/Antibody
PCH
Eu
DAPI
Measure mean intensity on PCH and euchromatic regions
Calculate ratio of intensity on PCH over euchromatin (Eu)
Hp1β
Fluorescence Ratio PCH/Eu
***
wild-type (757)
Suv39h dn (1047)

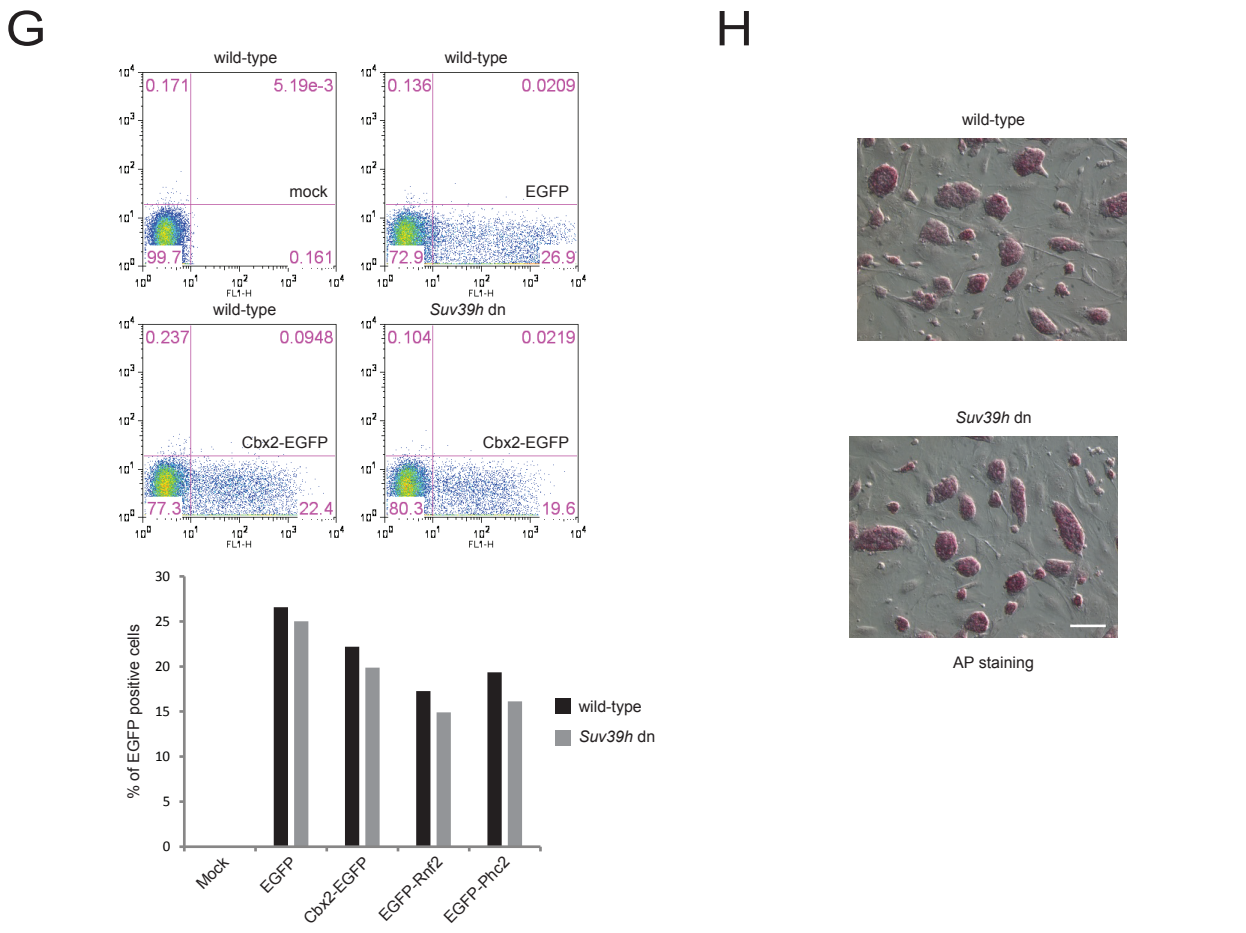

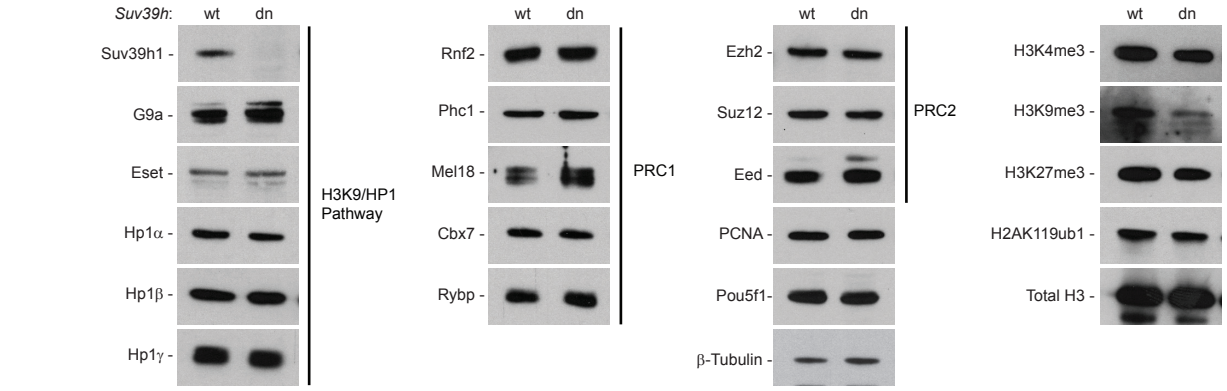

Figure S1 (related to Figure 1).

(A) Plots showing expression data of cPRC1, vPRC1, *Rnf2* and *Ring1* subunits during mouse early embryonic development. Expression of *Zp3*, *Pouf51* and *Hnrnpr* are shown as reference. Data were extracted from RNA-sequencing performed in oocytes (Oo), 1-Cell (C1), 2-Cell (C2), and 4-Cell (C4) stage and represented as Log2 of RPKM (Park et al., 2013).

(B) Western blot analysis showing the specificity of the Rybp antibody used in Figure 1B. Mouse ESCs were treated with siRNA against *Rybp* (siRybp-1, siRybp-2, siRybp-3, or a mixture of the 3 siRNA: siRybp-1-2-3) or transfected with an EGFP tagged Rybp. Endogenous (endo) Rybp protein levels decrease in cells transfected with *Rybp* siRNAs, compared to control siRNA (siSCR). The Rybp antibody can detect exogenous (exo) Rybp-EGFP (asterisk indicates degradation product). The Rybp antibody was a kind gift from M. Vidal.

(C) Rybp IF of mouse ESCs expressing a control (siSCR) or *Rybp* (siRybp-1) siRNA.

(D) Rybp IF of mouse ESCs transiently expressing an EGFP tagged Rybp.

(E) IF for H2AK119ub1 and 5mC in wild-type zygotes (n=12). Paternal PCH is labelled for both H2AK119ub1 and 5mC (white arrow).

(F) Scheme of the method used for scoring and representing the data from the automatic quantification of the immunofluorescence (IF) signal in ESCs. IF images are scanned with an in-house developed software (programmed in Matlab) that first identifies EGFP or antibody staining positive cells. Then, in each positive cells, masks are created using the DAPI staining to identify PCH and euchromatic regions (Eu) within the nucleus. Using these previously defined regions, mean intensity of fluorescence are measured in PCH and Eu and a ratio is calculated for each individual cell. Data are then plotted with SigmaPlot and the results are tested for significance with the Mann-Whitney Rank Sum Test. As an example, scoring of the IF signal of Hp1β in wild-type and *Suv39h* dn ESCs is shown.

(G) FACS analysis of the EGFP signal in wild-type and *Suv39h* dn ESCs transiently transfected with the indicated proteins. Representative FACS plots used for quantification of the EGFP signal from mock and transfected cells are shown (upper panel). A histogram shows the percentage of EGFP positive cells for the indicated proteins (lower panel). Results from wild-type and *Suv39h* dn ESCs are shown in black and grey respectively.

(H) Alkaline Phosphatase (AP) staining of wild-type and *Suv39h* dn ESCs.

(I) Western blotting of proteins from the H3K9/HP1 and Polycomb (PRC1 and PRC2) pathways and related histone modifications in wild-type and *Suv39h* dn ESCs.

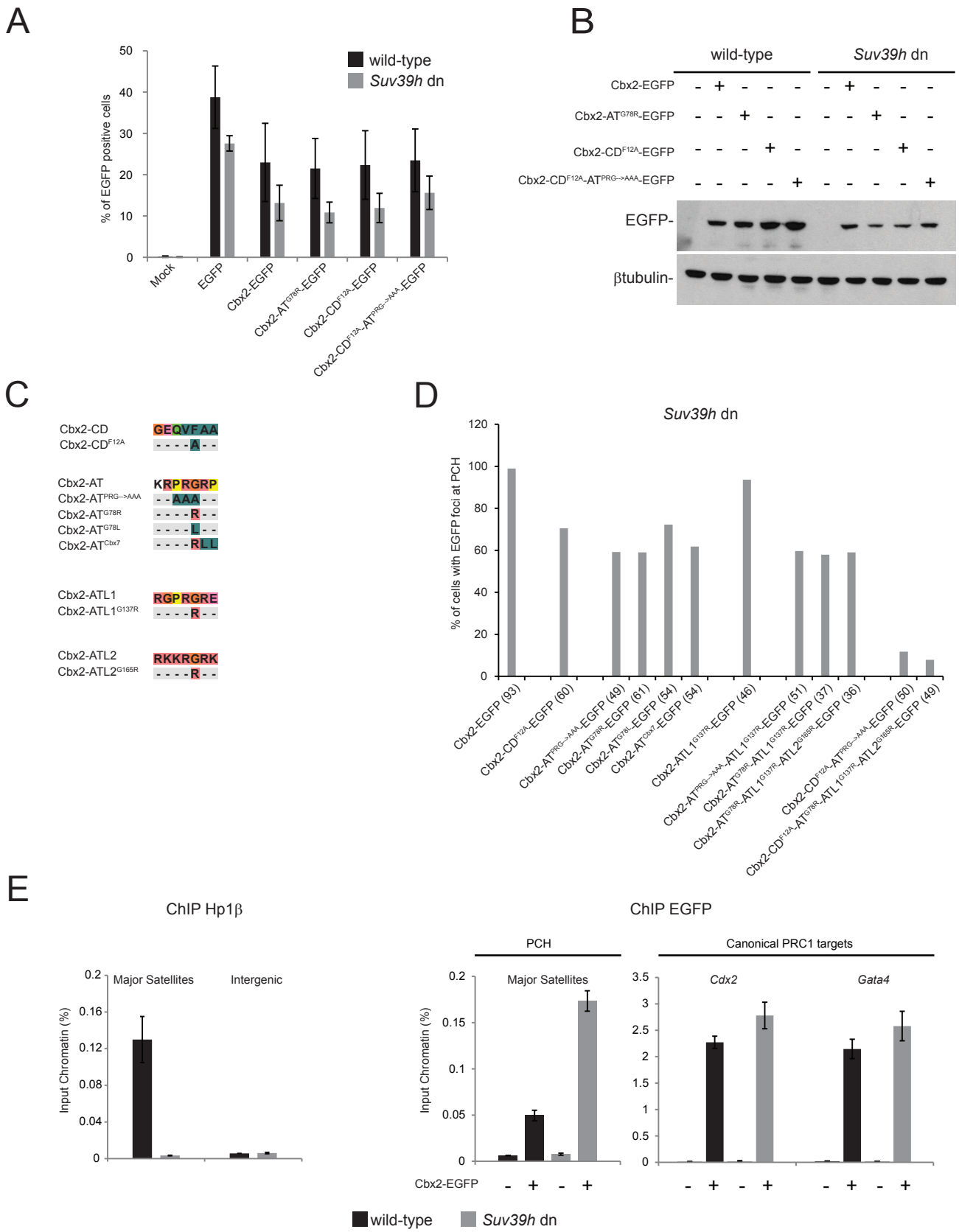

Figure S2 (related to Figure 2).
(A) Histogram for FACS analysis of wild-type and *Suv39h* dn ESCs transiently expressing the indicated EGFP-tagged full length Cbx2 constructs.
(B) Western blotting of full-length Cbx2 and point mutant constructs in wild-type and *Suv39h* dn ESCs. Cbx2 constructs were transiently transfected in ESCs before detection with a GFP antibody. Lower Cbx2-EGFP protein levels in unsorted population of *Suv39h* dn ESCs reflects lower frequencies of transfection (Figure S2A) rather than differential expression levels between individual wild-type versus *Suv39h* dn ESCs. β-Tubulin is used as a loading control.
(C) Mutations introduced into the chromodomain, AT-hook and ATL motifs of Cbx2.
(D) Classic quantification of enrichment of different Cbx2-EGFP constructs at PCH relative to euchromatin in *Suv39h* dn ESCs nuclei (shown as % of EGFP positive cells showing enrichment on PCH). Numbers in brackets refer to numbers of cells scored.
(E) Chromatin immunoprecipitation (ChIP) controls in wild-type and *Suv39h* dn ESCs. Hp1β binding to major satellites is impaired in *Suv39h* dn ESCs, as expected. Cbx2-EGFP binds the promoter of *Cdx2* and *Gata4* in both wild-type and *Suv39h* dn ESCs. Cbx2-EGFP binds strongly to major satellites in *Suv39h* dn ESCs compared to wild-type cells. Primers used to amplify mouse major satellite DNA (Martens et al., 2005; Peters et al., 2003), or regions 300bp and 400bp upstream of the TSS of *Cdx2* and *Gata4* respectively (Alder et al., 2010) were previously described. Results from wild-type and *Suv39h* dn ESCs are shown in black and grey respectively.

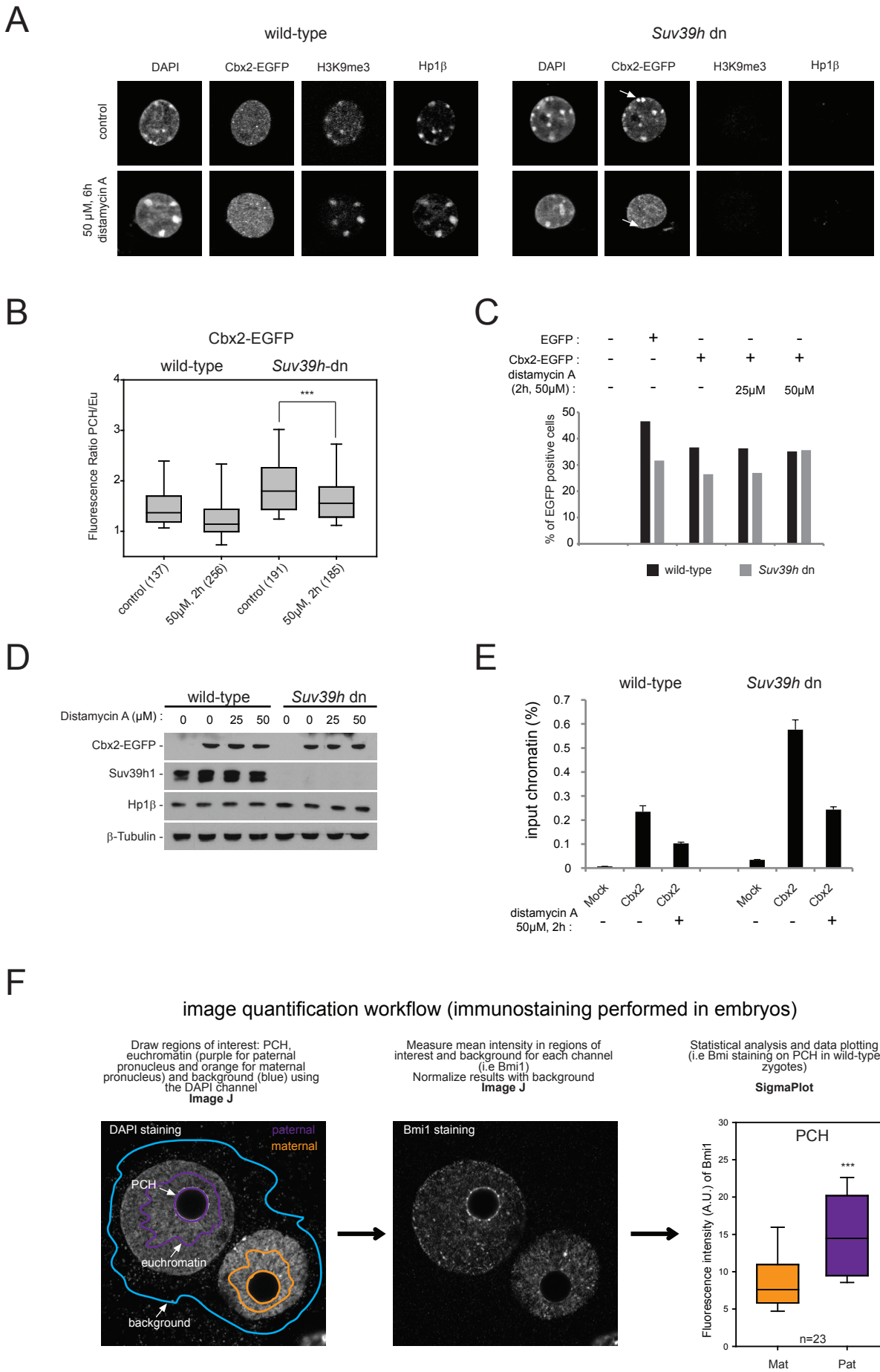
A
wild-type
Suv39h dn
DAPI
Cbx2-EGFP
H3K9me3
Hp1β
control
50 µM, 6h distamycin A
B
Cbx2-EGFP
wild-type
Suv39h-dn
Fluorescence Ratio PCH/Eu
***
control (137)
50µM, 2h (256)
control (191)
50µM, 2h (185)
C
EGFP :
Cbx2-EGFP :
distamycin A (2h, 50µM) :
25µM
50µM
% of EGFP positive cells
wild-type
Suv39h dn
D
wild-type
Suv39h dn
Distamycin A (µM) :
Cbx2-EGFP
Suv39h1
Hp1β
β-Tubulin
E
wild-type
Suv39h dn
input chromatin (%)
Mock
Cbx2
distamycin A 50µM, 2h :
F
image quantification workflow (immunostaining performed in embryos)
Draw regions of interest: PCH, euchromatin (purple for paternal pronucleus and orange for maternal pronucleus) and background (blue) using the DAPI channel
Image J
Measure mean intensity in regions of interest and background for each channel (i.e Bmi1)
Normalize results with background
Image J
Statistical analysis and data plotting (i.e Bmi staining on PCH in wild-type zygotes)
SigmaPlot
DAPI staining
paternal
maternal
PCH
euchromatin
background
Bmi1 staining
PCH
Fluorescence intensity (A.U.) of Bmi1
n=23
Mat
Pat

Figure S3 (related to Figure 3).
(A) Distamycin A treatment results in loss of Cbx2-EGFP enrichment at chromocenters in *Suv39h* dn ESCs. In wild-type cells, distamycin A treatment does not impair H3K9me3 and Hp1β localization. Representative picture of control and distamycin A-treated wild-type and *Suv39h* dn ESCs are shown.
(B) Quantification of enrichment of Cbx2-EGFP at PCH relative to euchromatin in wild-type and *Suv39h* dn ESCs treated with 50μM distamycin A for 2hr.
(C) Histogram for FACS analysis of the EGFP signal in wild-type and *Suv39h* dn ESCs transiently transfected with Cbx2-EGFP -/+ treatment with distamycin A. Results from wild-type and *Suv39h* dn ESCs are shown in black and grey respectively.
(D) Western blotting analysis shows that the presence of distamycin A does not alter Cbx2-EGFP nor Hp1β protein stability in both wild-type and *Suv39h* dn ESCs. βtubulin is used as a loading control.
(E) Histogram for EGFP ChIP-qPCR analysis of mouse major satellite repeats in wild-type and *Suv39h* dn ESCs upon transient transfection with Cbx2 (full length) –EGFP ± distamycin A treatment. Data are represented as percent of input chromatin. Error bars represent SD.
(F) Scheme of the method used for scoring and representing the data from immunostaining in zygotes. Using Image J (National Institute of Health), we identify and draw regions of interest: PCH, euchromatin and background from the DAPI channel. The mean intensity of fluorescence of PCH and euchromatin is then measured in each channel from non-saturated images and normalized to background. The resulting fluorescence intensities, indicated as arbitrary units (A.U.), are plotted using SigmaPlot and the results are tested for significance with the Mann-Whitney Rank Sum Test. As an example, scoring of the IF signal of Bmi1 at PCH in wild-type zygotes is shown. As expected Bmi1 is significantly more localized to pat-PCH, than mat-PCH.
***p≤0.001; ns: not significant. Numbers in brackets refer to number of cells or embryos scored.

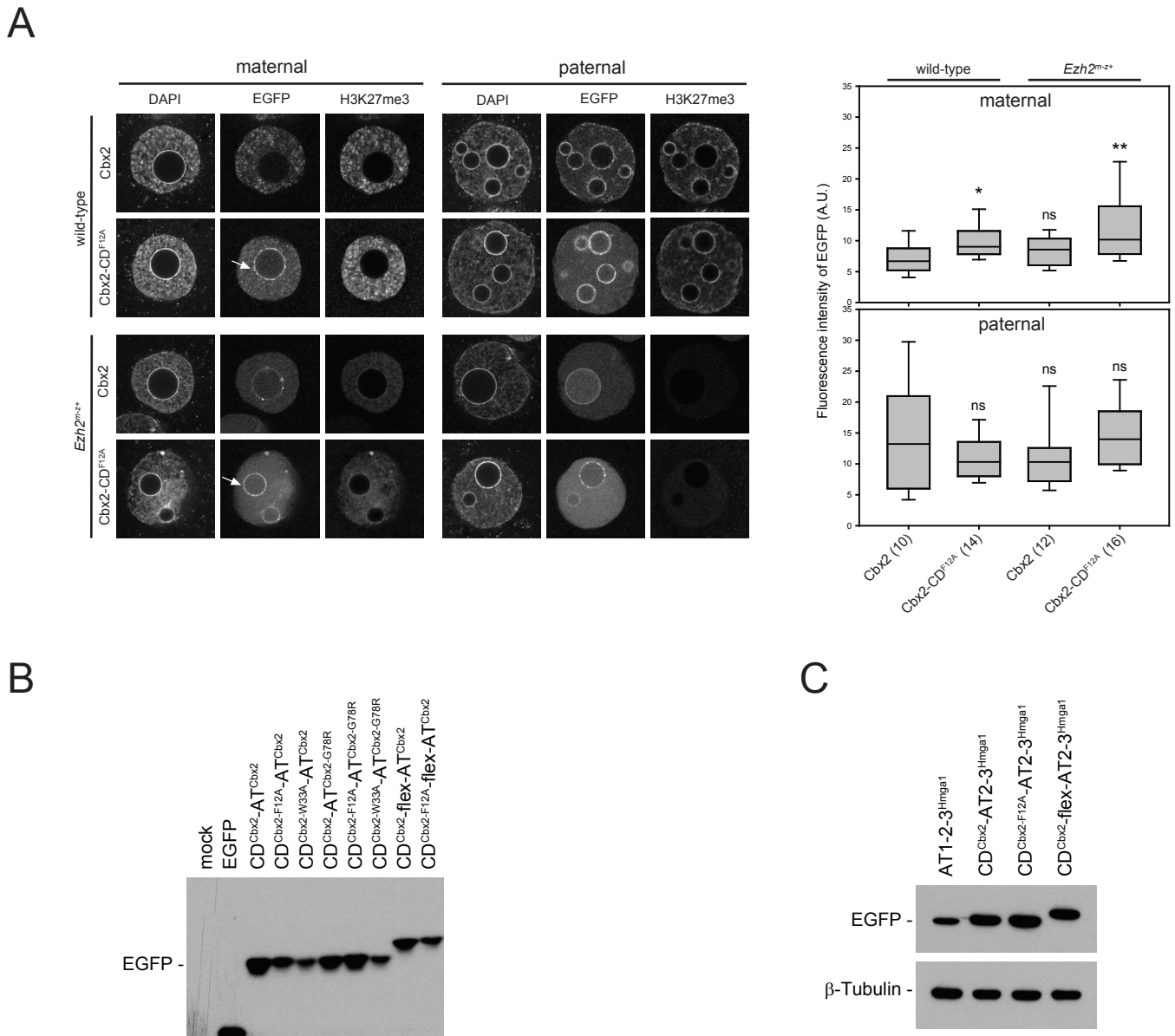

Figure S4 (related to Figure 5).

(A) Localization of Cbx2-EGFP and Cbx2-CD^{F12A}-EGFP constructs in maternal and paternal pronuclei of wild-type and *Ezh2* maternally deficient (*Ezh2*$^{m-z+}$) z**y**gotes (left panel). Box plots show quantification of EGFP fluorescence intensity at mat-PCH and pat-PCH for each construct (right panel).

(B) Western blotting of Cbx2-EGFP short reporter and point mutant constructs in ESCs. Cbx2 reporter constructs were transiently transfected in ESCs before detection with a GFP antibody. β-Tubulin is used as a loading control.

(C) Western blotting of CD^{Cbx2} and AT^{Hmga1} fusion proteins and point mutant constructs in ESCs. Cells were transiently transfected with the indicated constructs. Fusion proteins were detected with a GFP antibody. β-Tubulin is used as a loading control.

*p<0.05; **p≤0.01; ns: not significant. The number of embryos analyzed is shown between brackets.

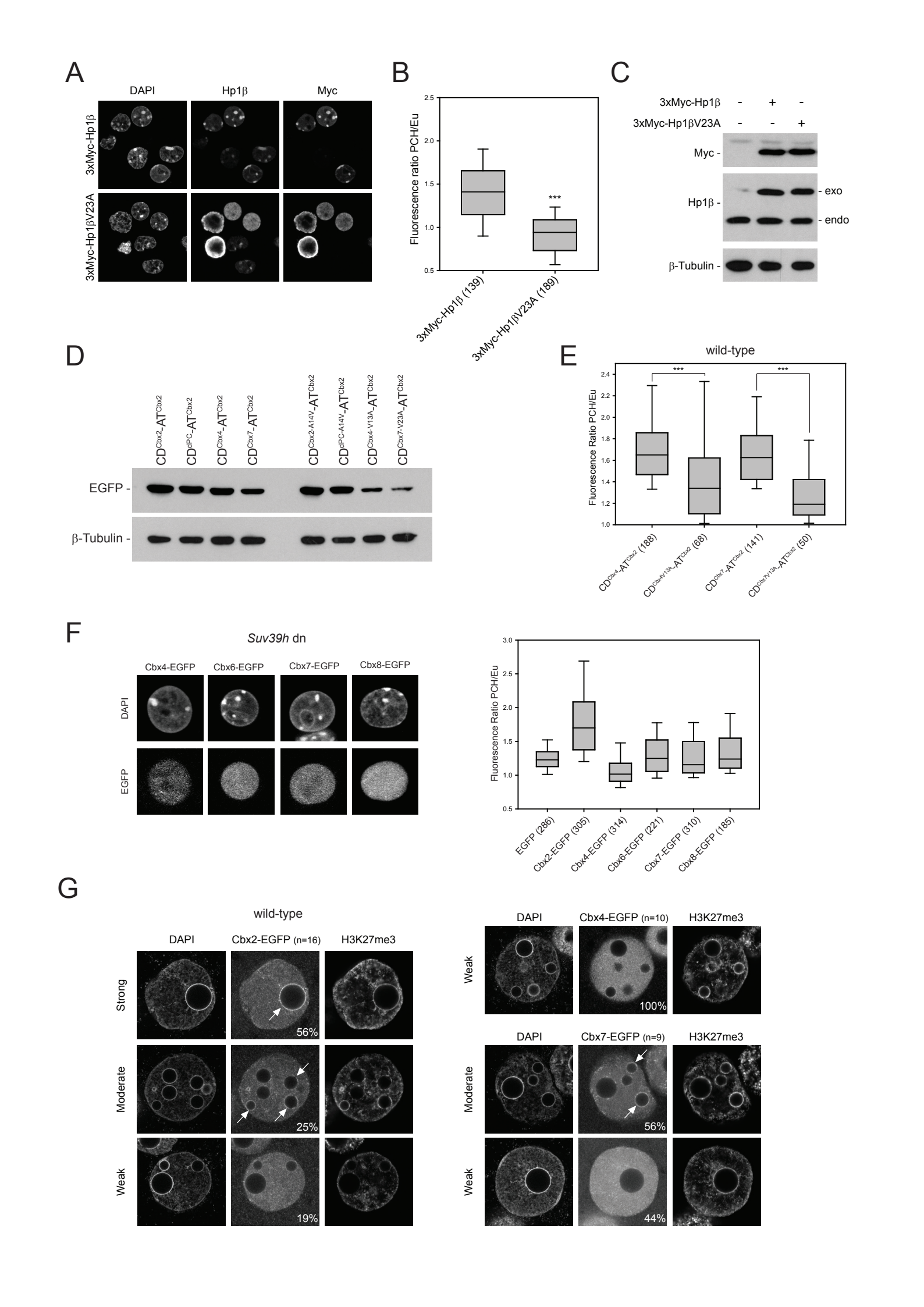
A
DAPI
Hp1β
Myc
3xMyc-Hp1β
3xMyc-Hp1βV23A
B
Fluorescence ratio PCH/Eu
***
3xMyc-Hp1β (139)
3xMyc-Hp1βV23A (189)
C
3xMyc-Hp1β - + -
3xMyc-Hp1βV23A - - +
Myc -
Hp1β -
- exo
- endo
β-Tubulin -
D
CDCbx2-ATCbx2
CDdPC-ATCbx2
CDCbx4-ATCbx2
CDCbx7-ATCbx2
CDCbx2-A14V-ATCbx2
CDdPC-A14V-ATCbx2
CDCbx4-V13A-ATCbx2
CDCbx7-V23A-ATCbx2
EGFP -
β-Tubulin -
E
wild-type
Fluorescence Ratio PCH/Eu
***
***
CDCbx4-ATCbx2 (188)
CDCbx4V13A-ATCbx2 (68)
CDCbx7-ATCbx2 (141)
CDCbx7V13A-ATCbx2 (50)
F
Suv39h dn
Cbx4-EGFP
Cbx6-EGFP
Cbx7-EGFP
Cbx8-EGFP
DAPI
EGFP
Fluorescence Ratio PCH/Eu
EGFP (286)
Cbx2-EGFP (305)
Cbx4-EGFP (314)
Cbx6-EGFP (221)
Cbx7-EGFP (310)
Cbx8-EGFP (185)
G
wild-type
DAPI
Cbx2-EGFP (n=16)
H3K27me3
Strong
Moderate
Weak
56%
25%
19%
DAPI
Cbx4-EGFP (n=10)
H3K27me3
Weak
100%
DAPI
Cbx7-EGFP (n=9)
H3K27me3
Moderate
Weak
56%
44%

Figure S5 (related to Figure 6).
(A) IF localization of 3xMyc-Hp1β and 3xMyc-Hp1βV23A in mouse ESCs transiently transfected with the indicated constructs.
(B) Quantification of the enrichment of exogenous Hp1β proteins (Myc-tag IF) on PCH shown in (A).
(C) Western blot analysis of mouse ESCs transiently transfected with the indicated Hp1β constructs. β-Tubulin is used as a loading control.
(D) Western blotting of the chimeric EGFP short reporter and point mutant constructs in ESCs. Cells were transiently transfected with the indicated constructs. Fusion proteins were detected with a GFP antibody. β-Tubulin is used as a loading control.
(E) Quantification of PCH enrichment of chimeric EGFP reporters containing the CD of Cbx4 or Cbx7 fused to AT^{Cbx2}. The Valine to Alanine mutation impairs PCH localization of Cbx4 and Cbx7 reporters in wild-type ESCs.
(F) EGFP localization of Cbx4-, Cbx6-, Cbx7- and Cbx8-EGFP fusion proteins in *Suv39h* dn ESCs (left panel). Quantification of the enrichment of exogenous EGFP tagged Cbx proteins on PCH in *Suv39h* dn ESCs (right panel).
(G) Localization of Cbx2, Cbx4 and Cbx7 EGFP constructs in paternal PCH and euchromatin of wild-type zygotes.
Numbers in brackets refer to number of cells scored (***p≤0.001).

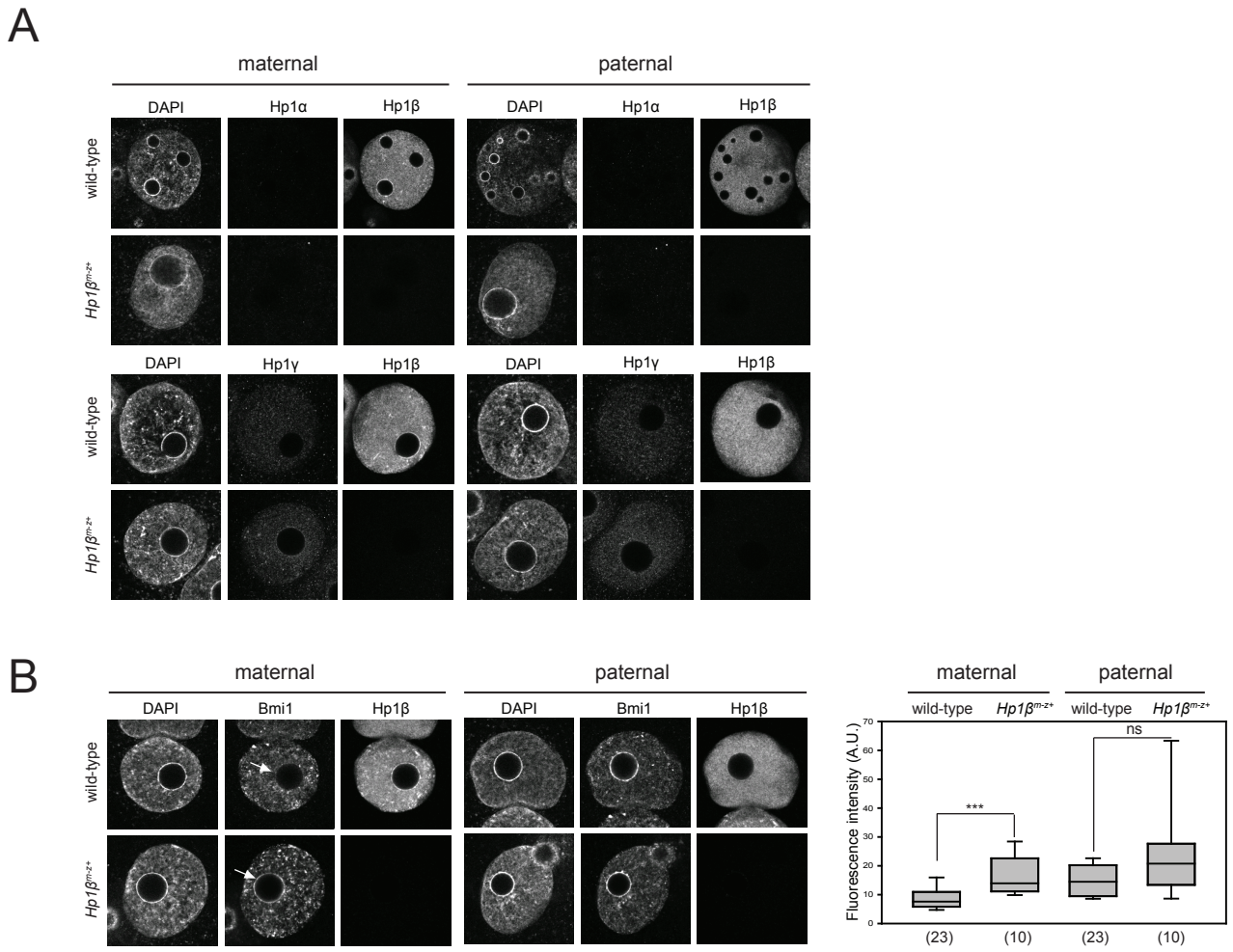
A
maternal
paternal
DAPI
Hp1α
Hp1β
Hp1γ
wild-type
Hp1β m-z+
B
maternal
paternal
Bmi1
Fluorescence intensity (A.U.)
wild-type
Hp1β m-z+
ns
***
(23)
(10)
C
H3K9me3
wild-type (26)
Hp1β m-z+ (17)
D
H4K20me3
wild-type (11)
Hp1β m-z+ (7)
**
E
Cbx2-EGFP
83%
97%
Suv4-20h dn
F

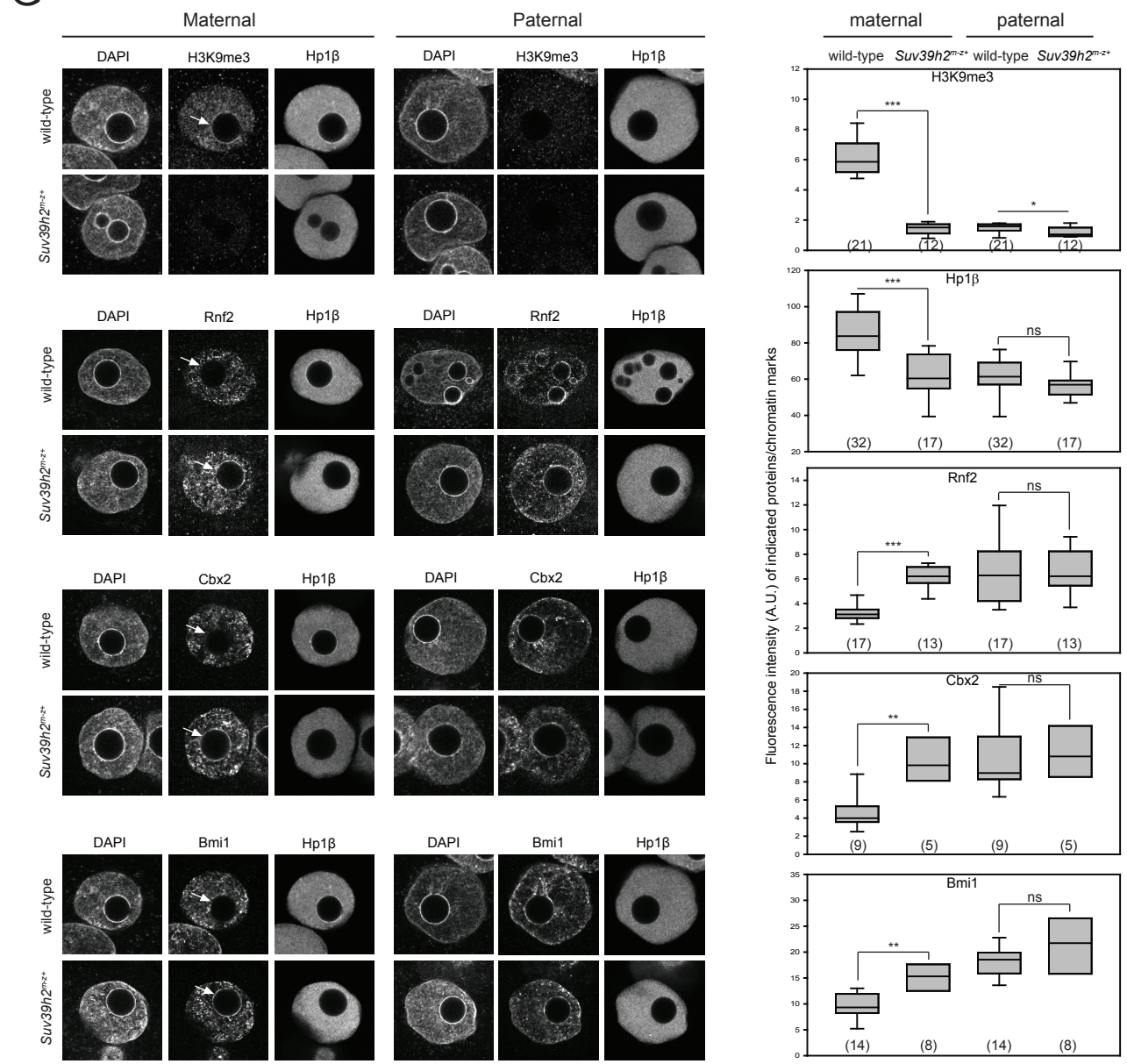

Figure S6 (related to Figure 7).
(A) IF analyses showing that expression levels and localization of Hp1α and Hp1β proteins are not changed in *Hp1*β$^{m\text{-}z+}$ compared to wild-type PN5 zygotes.
(B) IF localization of Bmi1 at PCH in maternal and paternal pronuclei of *Hp1*β$^{m\text{-}z+}$ zygotes compared to wild-type (arrows). Box plots show the quantification of fluorescence intensity for Bmi1 at mat-PCH and pat-PCH in wild-type and *Hp1*β$^{m\text{-}z+}$ zygotes.
(C, D) IF analyses show absence of anti-Hp1β signal and reduced levels for maternally inherited H4K20me3 in *Hp1*β$^{m\text{-}z+}$ versus wild-type zygotes. H3K9me3 levels are comparable between genotypes. Box plots show quantification of fluorescence intensity for indicated antibodies at mat-PCH in wild-type and *Hp1*β$^{m\text{-}z+}$ zygotes.
(E, F) IF localization of Cbx2-EGFP, H4K20me3 and Hp1β in wild-type and *Suv4-20h* dn ESCs. Percentages indicate cells that display the depicted phenotype.
(G) IF analyses showing that matPRC1 components Cbx2, Rnf2, and Bmi1 are enriched at mat-PCH in *Suv39h2*$^{m\text{-}z+}$ zygotes but not in wild-type PN5 zygotes (arrows). Box plots show quantification of fluorescence intensity for the indicated antibodies at mat-PCH and pat-PCH in wild-type and *Suv39h2*$^{m\text{-}z+}$ zygotes.
*p≤0.05; **p≤0.01; ***p≤0.001; ns: not significant. The number of embryos analyzed is shown between brackets.

Table S1: List of antibodies used in this study.

	Antibody	Origin	Ref	WB	IF	ChIP
PRC1	Bmi1	Upstate	05-637		1:200	
	Rnf2/Ring1b	Active Motif	39663	1:1000	1:300	
	Cbx2	A.Otte			1:300	
	Phc1	SIGMA	HPA006973	1:1000		
	Phc1	Active Motif	39724		1:300	
	Phc2	H.Koseki			1:200	
	Cbx7	Abcam	ab21873	1:1000	1:300	
	Rybp	Abcam	ab5976	1:2000		
	Rybp	M.Vidal		1:2000	1:500	
	H2AK119ub1	Cell Signaling	8240	1:2000	1:500	
PRC2	Ezh2	Cell Signaling	5246	1:1000		
	Suz12	Cell Signaling	3737	1:1000		
	EED	A.Otte		1:1000		
	H3K27me3	Upstate	07-449	1:1000	1:500	
	H3K27me3	Active Motif	39156	1:1000	1:500	
H3K9/HP1	Suv39h1	Cell Signaling	8729	1:1000		
	ESET	Upstate	07-378	1:1000		
	G9a	Cell Signaling	3306	1:1000		
	Hp1α	Euromedex	2HP-2G9-AS	1:1000	1:300	
	Hp1β	Serotec	MCA 1946	1:1000	1:500	4µg
	Hp1γ	Euromedex	2MOD-1G6-AS	1:1000	1:300	
	H3K9me3	Upstate	07-442	1:1000		
	H3K9me3	IMP			1:500	
	H4K20me3	IMP			1:500	
	5mC	Eurogentec	BI-MECY-0100		1:400	
Controls	GFP	Roche	11814460001	1:1000	1:200	4µg
	H3K4me3	Upstate	07-473	1:1000		
	βtubulin	SIGMA	T 4026	1:5000		
	Lamin A/C	Santa Cruz	SC6215	1:3000		
	PCNA	Santa Cruz	sc-56	1:1000		
	Pou5f1	BD Bioscience	611202	1:2000	1:500	
	H3	Abcam	1791	1:10000		

Supplemental Experimental Procedures

Constructs

For site-directed mutagenesis, approximately 25bp long primers containing the mutation in the center were used for amplification with Phusion Taq (Finnzymes). The PCR reaction was digested with the methylation sensitive restriction enzyme Dpn1 (New England BioLabs) to remove the original construct and subsequently used for transformation. Successful mutagenesis was confirmed by sequencing. The Cbx2 truncation constructs were generated by PCR from the Cbx2-EGFP construct. For the Cbx4, Cbx7 CD fusion constructs with the Cbx2 AT-hook, a Pst1 site was introduced between the CD of Cbx2 and the Cbx2 AT-hook for cloning. The CDs of Cbx4 and Cbx7 were amplified by PCR.

Cloning, expression and purification of Cbx proteins.

Cbx2 (9-66), Cbx2 (9-88), Cbx4 (8-65) and Cbx7 (8-62) were obtained as described before (Kaustov et al., 2011). Cbx2 (9-66)-A14V, Cbx4 (8-65)-V13A and Cbx7 (8-62)-V13A mutations were made by QuickChange II XL site-directed mutagenesis kit (Stratagene) and confirmed by complete cDNA sequencing. Proteins for NMR samples were prepared in M9-defined medium supplemented with ^{15}N-Ammonium Chloride and D-$^{13}C_6$ glucose for uniformly ^{13}C,^{15}N labeled samples or with ^{13}C labeled biosynthetic precursors to generate ^{13}C labeled methyl groups of Ile, Leu, Val for ILV labeled samples, respectively (Kaustov et al., 2011; Tugarinov et al., 2006).

Mice and Cell Lines

To produce maternally deficient *HP1β* mice, *Cbx1*$^{F/F}$ mice that carried the Zp3-cre recombinase transgene were generated. Housing and handling of mice conformed to the Swiss Animal Protection Ordinance, chapter 1.

ESCs were cultured in either DMEM medium with 4.5 g/l glucose (Gibco) containing 15% FCS (fetal calf serum, Chemicon), penicillin, streptomycin, 2 mM L-glutamine, 0.1 mM β-mercaptoethanol, non-essential amino acids and 1mM sodium pyruvate (Gibco) or with knockout serum replacement (Invitrogen) in presence of GSK3β and MEK1 inhibitors (2i) (CHIR99021, 3µM and PD184352, 0.8µM respectively, Axon Medchem).

Transiently transfected ESCs were seeded after approximately 16h of culture on poly-L-lysine coated coverslips, fixed with PFA and mounted in Vectashield containing DAPI (Vector).

Phosphatase Alkaline staining was performed with the Alkaline Phosphatase Detection Kit (SCR004, Millipore) following manufacturer's instructions.

siRNA knock down in ESCs was performed using Lipofectamine following the manufacturer's instructions (Invitrogen). Briefly, 2.10^5 cells were transfected with 100 pmole of siRNA duplexes, and collected 2 days later for subsequent Western blot or IF analysis. siRNA were purchased from Microsynth (Switzerland). Sequences are available upon request.

Flow Cytometry

Transiently transfected cells were harvested with Trypsin, washed in PBS and resuspended in 500µL of PBS-0.2%Serum. EGFP expression was analyzed by a flow cytometer (FACSCalibur, Beckton Dickinson) using CellQuest software (Beckton Dickinson). Plots and quantification of EGFP positive cells were performed with FlowJo software (Tree Star).

Collection, *in vitro* fertilization (IVF), micro-injection and culture of mouse embryos

Isolation of oocytes, and embryos, generation of mRNA and micro-injection were done as previously described (Posfai et al., 2012; Puschendorf et al., 2008).

Mouse oocytes and embryos were derived from superovulated 5-10 week old females according to standard procedures (Hogan et al., 1994). For IVF, females were injected with PMSG (5U, Intervet) and 48h later with hCG (5U, Intervet). M-II oocytes were then collected 14h after hCG injection. Sperm was obtained from 10-16 week old control males. Capacitation was carried out in human tubular fluid (HTF, Millipore) containing 7.5 mg/ml BSA for 2h. IVF was performed in HTF containing 7.5 mg/ml BSA (Gibco) for 2h. Zygotes were substaged according to morphology of pronuclei using criteria as defined previously (Adenot et al., 1997). In brief, PN0 refers to embryos immediately after fertilization and PN5 refers to embryos with large pronuclei located centrally within the embryo. For distamycin A treated PN0 zygotes, fertilization was performed in HTF containing 7.5 mg/ml BSA supplemented with distamycin A (Sigma, #D6135) for 2h.

For in vitro transcription, the plasmids were linearized and the mMessage mMachine T7 kit (Ambion, AM1344) was used. The synthesized mRNA was diluted to the optimal concentration using nuclease-free water (Ambion, AM9937). 2-4 pL mRNA (100ng/µl) was microinjected into the cytoplasm of in vitro fertilized CD1 zygotes using the Eppendorf FemtoJet injector system. Zygotes were then cultured in KSOM medium plus amino acids (Chemicon) under a 5% CO2 atmosphere at 37ºC and fixed at late zygotic stages (PN5).

Fluorescence Recovery After Photobleaching

The *Suv39h* dn ESCs were transiently transfected using Lipofectamine. For imaging, cells were plated on Ibidi plates (Ibidi, Germany), grown 24 hours in ESC medium and imaged on a spinning disc confocal setup comprising an Olympus IX81 (Olympus, Japan) microscope equipped with a Yokogawa CSU-X1 scan head, a 491nm laser line, a PlanApo 100x/1.45 TIRFM oil immersion objective, an ASI MS-2000 with Z-piezo stage, a Semrock Di01-T488/568-13x15x0.5 dichroic, a Semrock FF01-525/40-25 emission filter and a Cascade II EM-CCD camera (Photometrics). The setup was enclosed in a heating box and temperature was set at 37°C and controlled with a “Box” element (Life Cell imaging, Basel). The sample was covered with a plate dispensing

humidified air containing 5% CO2 at a flux rate of 6 l/hour controlled with a “Brick” element (Life Cell imaging, Basel). Final pixel size was 94nm. FRAP was performed using a Rapp-Optoelectronic module equipped with a 473 laser. The results were analyzed using ImageJ.

Immunofluorescence Staining

Before fixation of embryos, the zona pellucida was removed by incubation in acidic tyrode for 30 seconds. Embryos were washed twice in FHM, fixed for 15 min in 4% paraformaldehyde in PBS (pH 7.4) and permeabilized with 0.2% Triton-X 100 in PBS at room temperature (RT). Fixed embryos were blocked at least 4 hours at RT in 0.1% Tween-20 in PBS containing 2% BSA and 5% normal goat serum, and were then incubated with primary antibodies in blocking solution overnight at 4ºC. For 5mC detection, embryos were incubated in 4N HCl for 10 min at room temperature followed by neutralization in Tris-HCl, pH 8.0, for 10 min before overnight incubation with the primary antibody. Embryos were washed three times for 30 min in 0.1% Tween-20 in PBS containing 2% BSA before application of secondary antibodies for 1 hour at RT followed by three washing steps for 30 min in 0.1% Tween-20 in PBS containing 2% BSA in the dark. Primary antibodies were used in combination with cross-absorbed Alexa 488-, 568-, or 633-coupled secondary antibodies (Molecular Probes). Embryos were mounted in Vectashield containing DAPI (Vector). Mouse ESCs were trypsinized and placed on poly-L-lysine coated coverslips for 10 min to attach. Cells were fixed in 2% paraformaldehyde in PBS (pH 7.4), permeabilized in 0.1% Triton-X 100 in 0.1% sodium citrate. ESCs were blocked for 30 min in 0.1% Tween-20 in PBS containing 2% BSA and 5% normal donkey serum at RT and stained as described above.

Microscopy and image analysis

Immunofluorescence stainings of embryos were analyzed using the laser scaning confocal microscopes LSM510 META (Zeiss; software: LSM Image Browser) and LSM 700 (Zeiss: software: ZEN). One confocal slice through the maximal radius of each pro-

nucleus was scanned. The images were projected using ImageJ. Quantification of the mean fluorescence intensity of PCH and euchromatin in embryos was performed with ImageJ and normalized to background (Figure S3F). Unbiased automatic quantifications of fluorescence intensities in ESCs were performed from tiled pictures comprising at least 64 images taken with a 40X/1.3 oil objective on a Zeiss LSM700 microscope. Images were subsequently analyzed with a custom Matlab (MathWorks) script developed in house. In a first step, the EGFP (or antibody) positive cells were identified using a k-means clustering method. Next, the corresponding DAPI channel was classified into PCH (high intensity in DAPI), euchromatin (medium intensity in DAPI) and background (low intensity in DAPI outside the cell). Mean fluorescence intensity from PCH- and euchromatic-identified regions were calculated for both the DAPI and EGFP channel. For each labeled cell, the ratio of fluorescence signals at PCH over euchromatic regions was calculated for both DAPI and EGFP channels. Numerical data was exported into Excel and plotting and statistical analysis of the immunofluorescence data were conducted with SigmaPlot (Systat Software). Mann-Whitney U tests were calculated.

Immunoblot Analysis

For immunoblot analysis, cells washed with PBS were lysed in Laemmli buffer (for histones, acid extraction was performed according to the Abcam protocol). After measuring protein quantity by Bradford, equal amounts of protein were resolved by SDS-PAGE, transferred to a nitrocellulose membrane (Biorad), and probed with a primary antibody overnight at 4ºC. Membranes were then incubated with the appropriate HRP-conjugated secondary antibodies (1:10000, Amersham). The immunoreactive bands were detected by chemiluminescence (Thermo Fisher Scientific).

Immunoprecipitation

Protein extracts were prepared as followed: 1 volume of cells was resuspended in 1 volume of low salt buffer (20 mM Hepes at pH 7.9, 10 mM KCl, 0.1% (v/v) NP40 and cocktail of protease inhibitors). The lysis mixture was incubated on ice for 10 min. Then,

1 volume of high salt buffer was added (20 mM Hepes at pH 7.9, 1 M KCl, 6 mM $MgCl_2$, 20% (v/v) glycerol). DNA was broken with a syringe and needle and the lysis mixture was sonicated with a Bioruptor (Diagenode), incubated 30 min at 4 °C and centrifuged for 5 min at 4 °C. Immunoprecipitation buffer (20mM Hepes at pH 7.9, 10 mM KCl, 1.5 mM $MgCl_2$, 0.2% (v/v) Tween20, 10% (v/v) glycerol and cocktail of protease inhibitors) used at 2x concentration, was added to the lysis mixture, before pre-clearing with 15µl of Dynabeads protein G (Invitrogen) for 1 h at 4 °C with rotation. After collection of the pre-cleared lysate, 4µg of mouse anti-GFP antibody (Roche) pre-attached to 15µL of Dynabeads protein G was added and allowed to precipitate overnight at 4 °C with rotation. Beads were collected, washed three times with 1 ml of 1x immunoprecipitation buffer, and resuspended in SDS buffer before immunoblot analysis. All buffer were supplemented with a cocktail of protease inhibitor (Complete Mini EDTA-free, Roche).

Small-scale biochemical fractionation

One day after transfection of ESCs with Cbx2-EGFP constructs, $10x10^6$ cells were collected and subcellular fractions were then prepared and analyzed by Western blot as previously described (Julien and Herr, 2004).

Chromatin immunoprecipitation

ChIP-qPCR from ESCs was performed according to previously described protocols with modifications (Mohn et al., 2008; Tardat et al., 2010). Cells were collected, washed in PBS and were cross-linked in PBS containing 1% formaldehyde for 10 min at room temperature. The Cross-linking reaction was stopped by addition of glycine (125mM) for 5 min at RT. Cells were then washed twice with cold PBS. Pellets were resuspended in 15 mL buffer 1 (10 mM Tris (pH 8.0), 10 mM EDTA, 0.5 mM EGTA, 0.25% Triton X-100) and twice in 15 mL buffer 2 (10 mM Tris (pH 8.0), 1 mM EDTA, 0.5 mM EGTA, 200 mM NaCl). Then cells were lysed in 1 mL lysis buffer (50 mM HEPES/KOH (pH 7.5), 500 mM NaCl, 1 mM EDTA, 1% Triton X-100, 0.1% DOC, 0.1% SDS, protease inhibitors) and incubated on ice for at least 1h. DNA was sheared with first a 10 sec pulse

using a Branson sonicator (amplitude 70%), then samples were aliquoted in 1.5mL Eppendorf tubes containing 250µL of lysate each prior to sonication with a Bioruptor (Diagenode) for 25-30 cycles. DNA fragments length (between 200-600bp on average) was checked on agarose gel stained with ethidium bromide. For the immunoprecipitation, we incubated between 30-50µg of chromatin overnight at 4 °C with 3-5µg of indicated antibodies (Table S1) pre-attached to 15µL of Dynabead protein G (Invitrogen). Beads were washed twice with 1 mL lysis buffer, once with 1 mL DOC buffer (10 mM Tris (pH 8.0), 0.25 M LiCl, 0.5% NP-40, 0.5% deoxycholate, 1 mM EDTA), once with 1mL TE buffer and bound chromatin was eluted in 1% SDS/0.1 M $NaHCO_3$. After RNase A treatment followed by proteinase K digestion, cross-linking was reversed by overnight incubation at 65 °C. DNA was purified with the MinElute PCR Purification Kit according to the manufacturer's instructions (Qiagen). ChIP experiments were performed at least three times from independent chromatin preparations, and quantitative PCR analyses of ChIP DNAs were performed in triplicate using a SYBR Green quantitative PCR kit (Invitrogen) and a ABI 7500 Fast or a ABI StepOnePlus apparatus (Applied Biosystems), under conditions standardized for each primer set (primers are available upon request). The amount of DNA in ChIP samples was extrapolated from standard curve analysis of chromatin DNA before immunoprecipitation (input chromatin).

Preparation of NCP with H3 methylated histone analog.

Methylated H3Kc27me3 histone was prepared as described previously (Simon et al., 2007). The 601-DNA (‘Widom’ DNA) was obtained from 32X plasmid which contains 32 repeats of the 601-DNA sequence which were cleaved using ECORv and then used for nucleosome reconstitution using salt-gradient dialysis method as described previously) (Dyer et al., 2004).

Fluorescence Polarization

Chromodomains of Cbx2 (9-66), Cbx4 (8-65) and Cbx7 (8-62) were amplified by PCR from the Mammalian Gene Collection clones and were subcloned into a modified

pET28a-LIC vector. The recombinant proteins and their corresponding mutants were overexpressed as N-terminal His6-tagged proteins at RT using E. coli BL21 (DE3) Codon plus RIL (Stratagene) as a host organism. These expressed proteins were purified by Talon (BD) affinity chromatography under native conditions and eluted with buffer containing 500 mM Imidazole followed by size exclusion chromatography using a HiLoad 26/60 Superdex-75 column (GE Healthcare). The proteins were monomeric in solution as determined by size exclusion chromatography. The final samples were prepared in buffer containing 20 mM Tris (pH 8), 250 mM NaCl, 1mM DTT, 1mM TCEP, 1 mM Benzamidine, and 0.5 mM PMSF.

The buffer used in the binding assays contained 20 mM Tris pH 8.0, 250 mM NaCl, 1 mM DTT, 5 mM β-mercaptoethanol, 1 mM Benzamidine, 1 mM PMSF, and 0.01% Tween-20. Fluorescence polarization assays were performed in 384 well plates using Synergy 2 microplate reader (BioTek, Vermont, USA). To determine Kd values, the data were fit to a hyperbolic function using SigmaPlot software (Systat Software, Inc., CA, USA).

NMR spectroscopy and data analysis

The sequence-specific assignments of backbone and side chain resonances of human Cbx2$^{CD\text{-}AT}$ were assigned using the ABACUS approach from peak lists derived manually from peak picked spectra using NMR data collected at high resolution from non-linearly sampled spectra and processed using multidimensional decomposition (Gutmanas et al., 2002; Orekhov et al., 2003). We obtained assignments for all Ile, Leu and Val methyl groups of Cbx2$^{CD\text{-}AT}$ (2 Ile, 3 Val and 9 Leu) which were then used for chemical shift mapping for a U-[^{15}N,^{2}H]-labeled Cbx2$^{CD\text{-}AT}$ sample with Ile, Leu and Val selectively labeled with ^{13}C. Chemical shift mapping of Cbx2$^{CD\text{-}AT}$ was measured from the [^{15}N,^{1}H] and [^{13}C,^{1}H] TROSY spectra of U-[^{15}N,^{1}H] or U-[^{15}N,^{2}H],Ileδ1-[$^{13}CH_3$], Leu,Val-[$^{13}CH_3$,$^{12}CD_3$]-labeled Cbx2$^{CD\text{-}AT}$, respectively at protein concentrations ranging from 0.15mM-0.45mM, alone and with aliquots of [^{2}H]-H3K27cme3-NCP (1:1, 1:2, and 1:3 molar ratios) or unlabeled H3K27me3 peptide (residues 19-33; 1:1, 1:3 and 1:6 molar ratios) until no further changes in chemical shifts were detected. The TROSY and HSQC

spectra were recorded at 25^0C in 90/10% H_2O/D_2O with 20 mM TRIS pH 7.7, 150 mM NaCl, 1mM benzamidine, 0.5mM phenylmethylsulfonyl fluoride, 3mM β-mercaptoethanol. NMR experiments were performed at 293K on 600 and 800 MHz Bruker Avance spectrometers equipped with cryoprobes. Composite chemical shift perturbation (CSP) values were calculated using the equations $\Delta(\delta^1H\text{-}^{15}N) = [(\Delta\delta^1H)^2 + (\Delta\delta^{15}N/5)^2]^{1/2}$ and $\Delta(\delta^1H\text{-}^{13}C) = [(\Delta\delta^1H)^2 + (\Delta\delta^{13}C/4)^2]^{1/2}$. The data were processed with NMRPipe (Delaglio et al., 1995) and analyzed with NMRView and Sparky software (Goddard et al., 2006).

Supplemental References

Adenot, P.G., Mercier, Y., Renard, J.P., and Thompson, E.M. (1997). Differential H4 acetylation of paternal and maternal chromatin precedes DNA replication and differential transcriptional activity in pronuclei of 1-cell mouse embryos. Dev. Camb. Engl. *124*, 4615–4625.

Alder, O., Lavial, F., Helness, A., Brookes, E., Pinho, S., Chandrashekran, A., Arnaud, P., Pombo, A., O'Neill, L., and Azuara, V. (2010). Ring1B and Suv39h1 delineate distinct chromatin states at bivalent genes during early mouse lineage commitment. Dev. Camb. Engl. *137*, 2483–2492.

Delaglio, F., Grzesiek, S., Vuister, G.W., Zhu, G., Pfeifer, J., and Bax, A. (1995). NMRPipe: a multidimensional spectral processing system based on UNIX pipes. J. Biomol. NMR *6*, 277–293.

Dyer, P.N., Edayathumangalam, R.S., White, C.L., Bao, Y., Chakravarthy, S., Muthurajan, U.M., and Luger, K. (2004). Reconstitution of nucleosome core particles from recombinant histones and DNA. Methods Enzymol. *375*, 23–44.

Goddard T.D., Kneller D.G. (2006) SPARKY 3, v.3.113, University of California, San Francisco

Gutmanas, A., Jarvoll, P., Orekhov, V.Y., and Billeter, M. (2002). Three-way decomposition of a complete 3D 15N-NOESY-HSQC. J. Biomol. NMR *24*, 191–201.

Hogan, B., Costantini, F., and Lacy, E. (1994). Manipulating the Mouse Embryo: A Laboratory Manual (Cold Spring Harbor Laboratory Press).

Julien, E., and Herr, W. (2004). A switch in mitotic histone H4 lysine 20 methylation status is linked to M phase defects upon loss of HCF-1. Mol. Cell *14*, 713–725.

Martens, J.H.A., O'Sullivan, R.J., Braunschweig, U., Opravil, S., Radolf, M., Steinlein, P., and Jenuwein, T. (2005). The profile of repeat-associated histone lysine methylation states in the mouse epigenome. EMBO J. *24*, 800–812.

Mohn, F., Weber, M., Rebhan, M., Roloff, T.C., Richter, J., Stadler, M.B., Bibel, M., and Schübeler, D. (2008). Lineage-specific polycomb targets and de novo DNA methylation define restriction and potential of neuronal progenitors. Mol. Cell *30*, 755–766.

Orekhov, V.Y., Ibraghimov, I., and Billeter, M. (2003). Optimizing resolution in multidimensional NMR by three-way decomposition. J. Biomol. NMR *27*, 165–173.

Simon, M.D., Chu, F., Racki, L.R., de la Cruz, C.C., Burlingame, A.L., Panning, B., Narlikar, G.J., and Shokat, K.M. (2007). The site-specific installation of methyl-lysine analogs into recombinant histones. Cell *128*, 1003–1012.

Tugarinov, V., Kanelis, V., and Kay, L.E. (2006). Isotope labeling strategies for the study of high-molecular-weight proteins by solution NMR spectroscopy. Nat. Protoc. *1*, 749–754.